The solubility of sulphur in hydrous rhyolitic melts.

Béatrice Clémente, Bruno Scaillet, Michel Pichavant

The Solubility of Sulphur in Hydrous Rhyolitic Melts

BEATRICE CLEMENTE, BRUNO SCAILLET AND MICHEL PICHAVANT

INSTITUT DES SCIENCES DE LA TERRE D'ORLEANS, CNRS, 1A RUE DE LA FEROLLERIE, F-45071 ORLEANS CEDEX 2, FRANCE

Experiments performed at 2 kbar, in the temperature range 800–1000°C, with *f*O2 between *NNO*-2.3 and *NNO*+2.9 (where NNO is the nickel–nickel oxide buffer), and varying amounts of sulphur added to hydrous metaluminous rhyolite bulk compositions, were used to constrain the solubility of sulphur in rhyolite melts. The results show that fS2 exerts a dominant control on the sulphur solubility in hydrous silicate melts and that, depending on *f*O2, a rhyolitic melt can reach sulphur contents close to 1000 ppm at high *f*S2. At *f*O2 below *NNO+1*, the addition of iron to a sulphurbearing rhyolite magma produces massive crystallization of pyrrhotite and does not enhance the sulphur solubility of the melt. For a given *f*O2, the melt-sulphur-content increases with fS_2. For fixed *f*O2 and *f*S2, temperature exerts a positive control on sulphur solubilities, at least for *f*O2 below *NNO+1*. The mole fraction of dissolved sulphur exhibits essentially linear dependence on fH_2S at low fO_2 and, although the experimental evidence is less clear, on fSO_2 at high fO_2. The minimum in sulphur solubility corresponds to the redox range where both fH_2S and fSO_2 are approximately equal. A thermodynamic model of sulphur solubility in hydrous rhyolite melts is derived assuming that total dissolved sulphur results from the additive effects of H_2S and SO_2 dissolution reactions. The model reproduces well the minimum of sulphur solubility at around *NNO+1*, in addition to the variation of the sulphide to sulphate ratio with *f*O2. A simple empirical model of sulphur solubility in rhyolitic melts is derived, and shows good correspondence between model and observations for high-silica rhyolites.

KEY WORDS : sulphur; solubility; rhyolite; thermodynamics; fO_2; fS_2

INTRODUCTION

Sulphur species are the most abundant magmatic volatiles, after H_2O and CO_2. Sulphur is also a major component of magmatic solid and melt phases (e.g. pyrrhotite, anhydrite, Fe–S–O liquid). Experiments performed at 1 atm on a wide variety of silicate liquid compositions have shown that sulphur solubility is a function of fO2, f S2, temperature and melt composition (Fincham & Richardson, 1954; Richardson & Fincham, 1956; Abraham & Richardson, 1960; Abraham et al., 1960; Haughton et al., 1974; Katsura & Nagashima, 1974; Shima & Naldrett, 1975; Buchanan & Nolan, 1979; O'Neill & Mavrogenes, 2002). Experimental studies in which fO2 varied significantly have shown that a minimum in sulphur solubility occurs at around NNO to NNO+1 (NNO being the Ni–NiO solid buffer assemblage) (see Carroll & Webster, 1994). Experimental studies carried out at high pressure (Carroll & Rutherford, 1985, 1987; Luhr, 1990) on hydrous andesitic to dacitic compositions have also shown a minimum in sulphur solubility in this

redox range. The effect of temperature on sulphur solubility has been studied, mostly at 1 atm (Richardson & Fincham, 1954; St Pierre&Chipman, 1956; Nagashima & Katsura, 1973; Katsura & Nagashima, 1974; Buchanan et al., 1983). These studies showed that for a constant SO_2 input in 1 atm gas furnaces [or constant absolute value of fS_2 for the study by Buchanan et al. (1983)], and a constant absolute value of fO_2, the sulphur solubility increases with temperature under reducing conditions (below NNO-1) and decreases when temperature increases under oxidizing conditions. Luhr (1990) observed a positive dependence of sulphur solubility on temperature under oxidizing conditions at high pressure, but fS_2 was not kept constant in these experiments. In fact, with the exception of Luhr (1990), most highpressure sulphur solubility experiments have been performed without the precise and systematic control of fS_2. This hinders the understanding of the control that fS_2 may have on sulphur solubility in hydrous silicate liquids, which, in turn, renders difficult any thermodynamic modeling of the sulphur solubility in silicate melts. To address this issue, we have determined the relationship between fO_2, fS_2, T (temperature) and XS (dissolved melt sulphur content) for rhyolitic compositions. We have used rhyolitic compositions primarily because itmakes it possible to work at relatively low temperatures ($\leq$1000°C), where accurate control of critical parameters (namely T, fO_2, fH_2O, and fS_2) is comparatively easy. In addition, sulphur solubility data on rhyolitic melts are still scarce (Carroll & Rutherford, 1987; Luhr, 1990; Baker & Rutherford, 1996a; Scaillet et al., 1998), and our study aims at filling this gap. Rhyolitic melts represent important compositional end-members in the evolution of S-rich intermediate to silicic magmas, such as those found in arc settings (e.g. Martel et al., 1998; Scaillet & Evans, 1999). Here, we present a detailed set of sulphur solubility data, acquired at between 800 and 1000°C at 2 kbar and under various fO_2 and fS_2. We emphasize how fS_2, fO_2 and T control the solubility of sulphur in rhyolitic melts and we derive both a thermodynamic and an empirical model for the solubility of sulphur in hydrous rhyolite melts.

EXPERIMENTAL TECHNIQUES

Apparatus

All experiments were performed in an internally heated pressure vessel (IHPV), working vertically using Ar–H_2 mixtures as the pressurizing medium (Scaillet et al., 1992). For reducing conditions and at 800 and 930°C, we used a Shaw membrane to measure the f H2 (Shaw, 1963; Scaillet et al., 1992), connected to a Protais gauge (accurate to 0.1 bar). For experiments performed at 1000°C, the experimental fH_2 was measured using Ni–Pd-based solid sensors [Taylor et al., 1992; Pownceby & O'Neill, 1994; see Scaillet & Evans (1999) for additional details]. Sensor capsules were prepared using Pt tubes, lined with ZrO_2 to prevent reaction between Pt and the sensor material. The sensors were sealed. For each experiment, we used two starting sensor compositions with different bulk Ni/Pd ratios. In all cases, both sensors gave nearly identical final compositions, tightly bracketing the experimental fO_2 (or fH_2). Temperature was measured with three sheathed chromel–alumel thermocouples, calibrated at 1 atm against the melting point of NaCl and is accurate to within $\pm$5°C. Pressure was monitored by a factory-calibrated Heise gauge, accurate to within 20 bar. All experiments were performed at 2 kbar, with run durations of between 6 and 9 days.

Quenching was accomplished by turning off the furnace power, with quench rates of around 100°C/min between 800 and 250°C.

Starting materials and capsule preparation

The experiments were performed with crushed anhydrous glasses of rhyolitic composition (Table 1), obtained by fusion of a synthetic gel at 1400°C and 1 atm. The compositions correspond to that of the interstitial glasses of the recent Mont Pelée andesites (P1 Plinian eruption, dated at 650 BP; Martel et al., 1998) and that of Mt Pinatubo 1991 dacite (Table 1). Experimental charges were prepared by weighing finely ground glass and elemental sulphur (S) into Au capsules. Between 5 and 6 wt% deionized and distilled H_2O was added, so as to reach conditions slightly below H_2O saturation for a system without sulphur under our experimental conditions. A preliminary study showed that the starting form of sulphur in the experimental charge (as elemental, pyrrhotite or anhydrite) has no detectable effect on the stability of sulphur-bearing phases. The addition of sulphur as anhydrite or pyrrhotite can, however, lead to an increase of the FeO_{tot} and CaO contents of the melt, eventually resulting in the crystallization of a silicate or oxide phase. Therefore, to avoid significant modifications of the starting glass composition as a result of the addition of elements other than sulphur, we used mainly elemental sulphur as starting material. Different concentrations of sulphur were used to generate different fS_2. In some charges, synthetic pyrrhotites of differing starting compositions (i.e. Fe/S atomic ratio) were used as a sulphur source, with the purpose of monitoring the kinetics of attainment of equilibrium fS_2. In addition, to investigate the role of iron on sulphur solubility in hydrous silicic melt, some charges were doped with magnetite. The bulk compositions of these magnetite-added charges are listed in Table 1. After quenching, the capsules were re-weighed, to check for leaks. They were then pierced under a binocular microscope, in order to detect a fluid phase, and any H_2S smell was noted. After complete opening, glass chips were mounted in epoxy resin and polished using diamond solutions for SEM and electron microprobe analyses.

Control of fO_2 and fS_2

Oxygen fugacity was varied between NNO-2.3 and NNO+2.9, by varying the fH_2 and fH_2O of the experiment. The sample capsules were always positioned near the Shaw membrane or near the sensor capsules. The fO_2 of any given charge was calculated through the water dissociation reaction

$$\mathrm{K_w} = \frac{f\mathrm{H_2} \times f\mathrm{O_2}^{1/2}}{f\mathrm{H_2O}}.$$

We determined the fH_2O in each charge from the water content of the glass, using the model of Burnham (1979).

	MP natural[1]	MP synthetic[2]	MP15VII[3]	MP16VII[3]	MP17VII[3]	MP18XII[3]	MP19XII[3]	Pinatubo[4]
SiO_2	75·65	75·92	70·43	71·60	71·47	72·06	72·06	78·29
Al_2O_3	12·97	13·10	12·15	12·35	12·33	12·43	12·43	12·85
FeO	2·15	2·00	9·09	7·59	7·75	6·99	6·99	1·06
MgO	0·34	0·32	0·29	0·29	0·29	0·29	0·29	0·20
CaO	2·26	2·58	2·39	2·43	2·43	2·45	2·45	1·31
Na_2O	4·34	4·14	3·84	3·90	3·93	3·93	3·93	3·29
K_2O	1·94	1·94	1·80	1·83	1·83	1·84	1·84	2·85
FeO/(FeO+MgO)	0·86	0·87	0·97	0·96	0·96	0·96	0·96	0·84

The compositions are recalculated to 100% anhydrous. Total iron is given as FeO.
[1]Natural interstitial glass composition of Mt Pelée andesite erupted in 1929 (Martel *et al.*, 1998). It also contains 0·26 wt % TiO_2 and 0·08 wt % MnO.
[2]Dry synthetic glass used in all non magnetite-doped charges.
[3]Magnetite-doped charges, obtained by mechanical mixture between the dry MP synthetic glass and stoichiometric magnetite.
[4]Dry synthetic glass similar to the Pinatubo 1991 dacite interstitial glass (Scaillet & Evans, 1999). It also contains 0·15 wt % TiO_2.

Table 1: Starting compositions (wt %)

For experiments performed with a Shaw membrane, the oxygen fugacity of a given charge was computed from equation (2), knowing the fH_2 of the experiment, the fH_2O of the charge and the equilibrium constant of the reaction, Kw (Robie et al., 1979). For experiments with solid sensors, the prevailing fH_2 was first computed from equation (2), using the sensor composition and the model of Pownceby & O'Neill (1994) and assuming that fH_2O in the sensor was that of pure H_2O. Then, the fO_2 of the charge was calculated with fH_2 and fH_2O from the model of Burnham (1979). It should be noted that the above approach in controlling fO_2 does not require the presence of a fluid phase in the charge. Equilibrium (1) can be either homogeneous, with all components dissolved in the melt, or heterogeneous, with components either in the melt or fluid phases. The uncertainty in fO_2 calculation depends on the uncertainties in temperature, fH_2 and fH_2O. Errors arising from uncertainties attached to either fH_2 (± 0.1 bar) or temperature (±5°C) measurements are minor, i.e. less than 0.01 log fO_2. In contrast, the uncertainty attached to fH_2O is the main source of error, as it depends both on the uncertainty of the determination of the melt H_2O content, which is, here, estimated using the by-difference method (see below), and on the accuracy of the thermodynamic model used to calculate H_2O fugacities from melt H_2O contents. An error of ±0.5 wt%in the melt H_2O content, which corresponds to the analytical uncertainty of most charges, translates into an error of c. 10% in fH_2O using the model of Burnham (1979), which, in turn, translates into an uncertainty of c. 0.2 log units in fO_2, if all other parameters are held constant. The error associated with the thermodynamic model is more difficult to evaluate. In this study, all melt compositions are rhyolitic (see below), with SiO2 contents in the range 75–79 wt % (anhydrous basis) and are, therefore, in a compositional domain that is well covered by existing thermodynamic models of H_2O solubility in silicate melts (see Zhang, 1999). Although it is well known that the Burnham model does not properly account for the actual water species in the melt, a recent compilation by Zhang (1999) has shown that, in terms of bulk water solubility, the Burnham model yields water contents almost identical to those obtained using speciation models (e.g. Stolper, 1982), at least up to 3 kbar. Thus, besides the speciation of water in silicate melt, the use of either model

(Burnham- or Stolper-type) makes no difference in terms of f H_2O calculations that we are interested in. The Burnham model is based on the thermodynamic properties of pure water, as determined by Burnham et al. (1969), which were also used to derive the a and b parameters used in the MRK equation of state (EOS) of H_2O by Holloway (1977). In the updated version of the Stolper model, provided by Zhang (1999), the EOS of Pitzer & Sterner (1994) is used to calculate fH_2O. As explained below, the MRK-EOS of Holloway (1977) is used for the calculation of fS_2. Therefore, for the sake of internal consistency, the Burnham model has been used in this work. Standard error propagation formalism of analytical or experimental sources of error through equation (2) yields an uncertainty in fO_2 that is always less than 0.6 log units and with an average ($\pm 1\sigma$) of 0.18 log units for all charges. All experimental fO_2 are referenced to the NNO buffer (Holloway et al., 1992).

The fS_2 was determined from the composition of pyrrhotite, crystallized during the experiment (Froese & Gunter, 1976). The fS_2 of the experiments was thus not fixed by a standard buffer assemblage such as pyrite–pyrrhotite, but, instead, it was a function of the initial amount of sulphur in the charge and of the imposed experimental conditions. By changing the bulk sulphur content of the starting material, we changed the fS_2 of the system. Sulphur fugacities calculated with pyrrhotite composition determined by XRD (see below) are known to within $\pm$ 0.2 log units. However, under oxidizing conditions, pyrrhotite is not a stable phase and is replaced either by an Fe–S–O liquid (see below) or by anhydrite (Carroll & Rutherford, 1985, 1987; Luhr, 1990). In our experiments, progressive addition of sulphur leads to saturation of the hydrous silicate liquid with respect to a fluid phase. In such cases (i.e. fluid phase present), we used an MRK equation of state (e.g. Holloway, 1977, 1981, 1987) to determine fS_2 and the fluid phase composition.

The fluid phase can be described in the H–O–S system. By the phase rule, we have

$$v = 2 + C - \varphi$$

where C is the number of components, φ is the number of phases and v is the degree of freedom (4 in this case). The pressure, the temperature and the fH_2 are fixed in our experiments and we know the ${}_fH_2O$ of each charge. Therefore, the system is invariant and we can calculate the fluid phase composition and, thus, the ${}_fS_2$. Note that this allows calculation of the fugacities of all S-bearing species in the fluid, even if none is known.

In this study, we used the MRK equation of state (MRK-EOS) of Holloway (1977):

$$P = \frac{RT}{V - b} - \frac{a}{\sqrt{T}\,(V^2 + Vb)}$$

P is the pressure, T the temperature,

where P is the pressure, T the temperature, V the volume, and a and b are two parameters as a function of temperature and/or pressure. For pure phases, a and b can be estimated from the critical pressure (Pc) and temperature (Tc) (Breedveld & Prausnitz, 1973; Ferry & Baumgartner, 1987). Calculation of the fluid phase compositions indicates that the major species under our experimental conditions are

H_2O, H_2, H_2S, SO_2 and S_2. H_2O is a polar molecule, the parameters *a* and *b* for water, taken from Holloway (1981). H_2S and SO_2 are also polar molecules but no P–V–T data are available under our experimental conditions. Therefore, we considered these molecules as non-polar, *a* and *b* being determined from *Pc* and *Tc*, as given by Shi & Saxena (1992). For S_2, *Pc* and *Tc* are not known and we used the estimated values of Shi & Saxena (1992). The full set of a and b parameters used in the MRK-EOS is listed in Table 2.

	a (atm × cm^{6}K$^{0.5}$/mole^2)	b (cm^3/mole)
H_2[1]	3.56×10^6	15.15
H_2S[2]	89.38×10^6	29.89
SO_2[2]	142.92×10^6	39.46
S_2[2]	25×10^6	20.57
	a_o	b
H_2O[1]	35×10^6	14.6

[1]From Holloway (1981).
[2]From Shi & Saxena (1992).

Table 2: a and b parameters used in the MRK equation of state

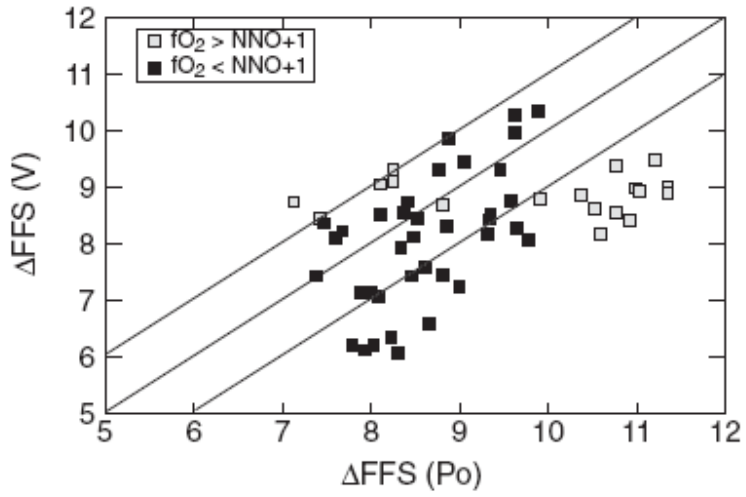

Fig. 1. Comparison between fS_2 measured by the pyrrhotite composition [DFFS(po)] and fS_2 calculated from an MRK equation of state [DFFS(V)].

The MRK program was checked against the program of Connolly & Cesare (1993) and, for given P, T, fH_2 and fH_2O conditions, both methods were found to agree within 0.2 log fS_2.

As discussed previously, for reducing conditions (fO2< NNO), fS_2 was calculated from the pyrrhotite composition. Some pyrrhotite-bearing charges that were saturated with a fluid phase provided a test of the validity of the MRK-EOS approach to compute fS_2 and fluid phase compositions. As shown in Fig. 1, the fS_2 given by the pyrrhotite composition and the fS_2 given by the fluid phase composition are usually found to agree with each other to within 1 log unit for most charges, which is considered encouraging, given our current poor knowledge of the thermodynamic behavior of the H–O–S fluids at magmatic conditions. Charges at an fO_2 above NNO+1 or at 1000°C are those for which the two methods yielded significantly different results (Fig. 1). This misfit could be due, in part, to the modification of sulphide composition during cooling (see below). Despite this limitation, we conclude that it is possible to use the MRK equation of state to estimate fS_2 of charges lacking pyrrhotite, at least for H_2O-rich fluid compositions. An additional check on the accuracy of the calculated fS_2 was also provided by comparing the H_2O/S ratio of the fluid phase, as calculated from MRK, against that obtained through mass balance. In the latter, the amount of S and H_2O left over for the fluid phase can be determined. Thus, the H_2O/S ratio of the fluid can be obtained and compared with H_2O/S values calculated from the MRK-EOS approach. Pyrrhotite-free charges for which the calculated H_2O/S ratios from both methods failed to converge were not considered for deriving either the thermodynamic or the empirical models of sulphur solubility presented below. Sulphur fugacities calculated using an MRK approach have larger associated uncertainties than those calculated from the pyrrhotite composition (around $\pm$ 0.5 log units), largely because of the propagation of the uncertainty associated with the determination of melt water contents. All values of fS_2 are referenced to the FFS buffer, which corresponds to the equilibrium between iron and troilite :

$$\mathrm{Fe} + \tfrac{1}{2}\mathrm{S_2} \Leftrightarrow \mathrm{FeS}$$

$$\ln f\,\mathrm{S_2} = \frac{2}{RT}(-0.2655(P-1) - 35910 + 12.56T)\ \text{(Froese \& Gunter, 1976)}$$

with T in K, P in bar and R in cal/mol K. We extrapolated the data from Froese & Gunter (1976) to high temperature (above 900°C) and, at 2 kbar, the -log fS_2 (FFS) is 9.36 at 800°C, 7.75 at 930°C and 7.02 at 1000°C. Knowing fH_2, fS_2, and fO_2, the equilibrium values of both fH_2S and fSO_2 were calculated using the following equilibria:

$$\tfrac{1}{2}\mathrm{S_2} + \mathrm{H_2} \Leftrightarrow \mathrm{H_2S}$$

$$\tfrac{1}{2}\mathrm{S_2} + \mathrm{O_2} \Leftrightarrow \mathrm{SO_2}$$

using the equilibrium constants of Ohmoto & Kerrick (1977).

Attainment of equilibrium

Kinetic studies performed by Turkdogan & Pearce (1963) on simultaneous oxidation and sulfidation reactions in anhydrous iron-bearing silicate liquids showed that sulfidation is faster than iron oxidation. The corresponding

	Po5	Po7
$d(_{102})$[1]	2·0815	2·0500
NFeS[2]	0·975	0·920
% at Fe[3]	48·77	45·97

[1]Distance between inter-reticular 102 plane of hexagonal pyrrhotite determined by XRD.
[2]Mole fraction of FeS in pyrrhotite from Toulmin & Barton (1964).
[3]Atomic proportion of Fe in pyrrhotite calculated after Yund & Hall (1969).

Table 3: Composition of synthetic pyrrhotites

two reactions are

$$\tfrac{1}{2}S_{2g} \Leftrightarrow S_m^{2-}$$

$$2FeO + \tfrac{1}{2}O_2 \Leftrightarrow Fe_2O_3.$$

Both the sulfidation and oxidation reactions are related through the following equilibrium:

$$\tfrac{1}{2}S_{2_g} + 2Fe_m^{2+} \Leftrightarrow 2Fe_m^{3+} + S_m^{2-}.$$

Baker & Rutherford (1996b) and Gaillard et al. (2001) have shown that the Fe^{3+}/Fe^{2+} ratio is constant after 24 h run durations for hydrous rhyolitic compositions, equilibrated between 725 and 1150°C, 100 and 2000 bar, and fO_2 between NNO and $MnO–Mn_2O_3$. Given that our run durations are between 6 and 9 days, we can expect that the iron redox ratio is at equilibrium and, consequently, that sulphur solubility is also at equilibrium. The Fe content of the capsules was always found to be below detection (270 ppm), even under reduced conditions. At fO_2 higher than NNO, sulphur-free supra-liquidus glasses have the same iron content as the starting composition. At lower fO_2, Fe loss occurred but remained negligible. The maximum Fe loss occurred at 1000°C, where the glass has an FeO content of 1.5 wt % (instead of 2 wt %). However, in all cases, Fe

concentration profiles toward the glass-capsules contact were flat in the glass, which suggests that equilibrium between melt and capsule was attained with respect to Fe. To check the attainment of the fS_2 equilibrium in some experiments, we added two additional capsules, where 1 wt % sulphur was added as synthetic pyrrhotite (Table 3). Two different pyrrhotites (charges with Po5 and Po7 in Table 4) were synthesized in evacuated SiO2-glass tubes (Kullerud, 1971) using iron and sulphur powder (both from Aldrich, 99.99% purity). For the synthesis, the sample was heated rapidly to 400°C, kept at this temperature over 12 h and then held at 700°C for 48 h. The compositions of the two synthetic pyrrhotites are given in Table 3. In the first capsule, the synthetic starting pyrrhotite was iron-rich [NFeS = 0.975; NFeS is the mole fraction of FeS in the system FeS–S_2 (Toulmin & Barton, 1964)] and, in the second one, the pyrrhotite was sulphur-rich (NFeS = 0.92). During the experiment, pyrrhotites in these two capsules re-equilibrated to the prevailing conditions, yielding final pyrrhotite compositions identical within error and suggesting attainment of equilibrium fS_2, as illustrated in Fig. 2 for the experiments MP10. In all pyrrhotite-bearing charges, the two sensor capsules yielded identical fS_2 (except when the prevailing fO_2 is outside the stability field of pyrrhotite, such as MP19 charges) and we conclude that f S2 is at equilibrium for all experiments presented here. Attainment of equilibrium conditions is corroborated by the compositional homogeneity of glasses, both for major (e.g. SiO_2) and minor element (S) concentrations.

Table 4: Experimental conditions and run products

Charges	wt % S[1]	aH_2O[2]	$\log fO_2$[3]	ΔNNO[4]	σ(102)[5]	at % Fe[6]	$\log fS_2$ (pol)[7]	$\log fS_2$ (V)[8]	ΔFFS (pol)[9]	ΔFFS (V)[10]	Gl	Pl	Px	Qz	Po	An	V
P = 2·152 kbar, T = 785° C, fH_2[11] = 2·74 bar, 143 h																	
MP15 I	1·18 (S)	0·81 (0·09)	−15·30 (0·13)	−1·12 (0·10)	2·0688	47·57	−2·14 (0·42)	−0·78 (0·50)	7·45 (0·21)	8·81 (0·25)	94·41 (3·43)	3·52 (1·77)	0·87 (0·51)	—	1·17	—	1·39 (0·50)
MP15 II	2·29 (S)	0·80 (0·29)	−15·34 (0·32)	−1·16 (0·29)	2·0532	46·23	−0·16 (0·38)	−0·53 (0·57)	9·43 (0·19)	9·06 (0·26)	74·99 (2·89)	14·38 (1·59)	0·95 (0·43)	8·30 (1·69)	1·37	—	3·25 (0·84)
MP15 III	3·72 (S)	0·37 (0·09)	−16·01 (0·30)	−1·83 (0·22)	2·0481	45·82	0·36 (0·37)	0·03 (0·09)	9·95 (0·19)	9·62 (0·06)	57·64 (2·33)	25·04 (1·27)	0·55 (0·40)	15·41 (8·51)	1·36	—	6·18 (0·36)
MP15 IV	5·69 (S)	0·35 (0·15)	−16·11 (0·54)	−1·93 (0·39)	2·0449	45·58	0·66 (0·37)	0·05 (0·14)	10·25 (0·18)	9·63 (0·10)	47·82 (2·12)	32·59 (1·31)	0·73 (0·42)	17·90 (1·17)	1·37	—	9·15 (0·44)
MP15 V	10·62 (S)	0·01	−17·65	−3·47	2·0441	45·52	0·73 (0·37)	0·29	10·32 (0·19)	9·88	53·59 (2·84)	26·77 (1·77)	1·89 (0·58)	16·82 (1·35)	0·92	—	15·23 (0·20)
MP15 VI	1·36 (po5—po7)	1·00	−14·84	−0·93	2·0760	48·23	−3·21 (0·13)	*−1·36 (0·30)*	6·19 (0·13)	*8·03 (0·30)*	95·60 (1·21)	4·30 (0·91)	—	—	0·10 (0·16)	—	1·06 (0·78)
MP15 VII[13]	3·70 (S)	1·00	−14·84	−0·93	2·0754	48·18	−3·23 (0·11)	—	6·36 (0·22)	—	90.74 (0·56)	—	—	—	9·26	—	—
MP15 X	1·02 (S)	0·92 (0·09)	−15·19 (0·11)	−1·03 (0·08)	2·0690	47·58	−2·17 (0·42)	−1·12 (0·22)	7·42 (0·21)	8·46 (0·14)	98·90 (1·21)	traces	—	—	1·10 (0·16)	—	3·21 (1·11)
MP15 XI	1·11 (S)	0·97 (0·03)	−15·14 (0·04)	−0·98 (0·09)	2·0708	47·75	−2·46 (0·43)	−1·60 (0·30)	7·13 (0·21)	7·99 (0·18)	98·89 (1·20)	—	—	—	1·11 (0·11)	—	5·05 (1·15)
MP15 SN	1·10 (S)	0·79 (0·18)	−15·34 (0·28)	−1·18 (0·20)	2·0702	47·69	−2·35 (0·42)	−0·59 (0·15)	7·24 (0·21)	9·00 (0·31)	96·42 (1·20)	1·73 (0·90)	0·56 (0·40)	—	1·27 (0·40)	—	2·67 (0·87)
PIN 15 VIII	3·62 (S)	0·78 (0·06)	−15·33 (0·09)	−1·16 (0·07)	2·0490	45·89	0·27 (0·38)	−0·71 (0·23)	9·86 (0·19)	8·88 (0·15)	62·99 (1·86)	20·30 (1·17)	—	15·77 (1·03)	0·94	—	5·23 (0·27)
P = 1·973 kbar, T = 786° C, fH_2[11] = 1·8 bar, 139 h																	
MP16 I	1·16 (S)	0·88 (0·13)	−12·59 (0·18)	1·30 (0·12)	2·0524	45·16	*0·00 (0·15)*	1·37 (0·31)	*9·39 (0·07)*	10·76 (0·19)	53·98 (1·81)	26·40 (0·97)	—	17·88 (1·14)	1·74	—	2·28 (0·48)
MP16 II	2·66 (S)	0·77 (0·12)	−12·71 (0·19)	1·18 (0·13)	2·0563	46·48	*−0·42 (0·15)*	1·61 (0·56)	*8·97 (0·08)*	10·99 (0·26)	41·67 (1·66)	34·02 (0·94)	—	22·40 (1·04)	1·9	traces	5·33 (0·29)
MP16 III	4·40 (S)	0·75 (0·12)	−12·73 (0·18)	1·16 (0·19)	2·0567	46·51	*−0·46 (0·19)*	1·66 (0·46)	*8·92 (0·10)*	11·04 (0·24)	36·30 (1·51)	36·71 (0·88)	—	25·11 (0·97)	1·88	—	7·14 (0·29)
MP16 IV	6·10 (S)	0·61 (0·09)	−12·91 (0·18)	0·98 (0·13)	2·0562	46·47	*−0·41 (0·16)*	1·97 (0·17)	*8·98 (0·08)*	11·35 (0·11)	29·66 (1·30)	41·97 (0·87)	—	26·46 (0·87)	1·9	—	9·30 (0·24)
MP16 V	10·74 (S)	0·67 (0·12)	−12·90 (0·12)	1·07 (0·16)	2·0570	46·54	*−0·50 (0·20)*	1·95 (0·12)	*8·89 (0·10)*	11·35 (0·08)	33·72 (1·50)	40·70 (0·96)	—	23·68 (0·94)	1·91	—	13·64 (0·30)
MP16 VII[13]	4·00 (S)	0·86	−12·60	1·29	2·0574	46·58	*−0·55 (0·15)*	0·99 (0·92)	*8·84 (0·80)*	10·38 (0·46)	79·20 (1·17)	11·20 (0·84)	—	—	6·80 (0·20)	—	4·48 (0·46)
MP16 VIII	1·11 (S)	0·98 (0·03)	−12·49 (0·04)	1·41 (0·09)	2·0608	46·67	−1·00 (0·30)	0·67 (0·94)	8·43 (0·10)	10·06 (0·30)	36·30 (1·51)	36·71 (0·88)	—	25·11 (0·97)	1·88	—	7·14 (0·29)
MP16 IX	1·37 (S)	0·98 (0·02)	−12·48 (0·08)	1·41 (0·02)	2·0583	46·65	−0·70 (0·30)	0·69 (0·63)	8·73 (0·10)	10·08 (0·27)	57·46 (2·02)	21·04 (1·10)	—	20·21 (1·16)	1·29 (0·16)	—	6·64 (0·29)
PIN16 VI	4·39 (S)	0·68 (0·10)	−12·80 (0·18)	1·08 (0·13)	2·0516	46·10	0·08 (0·30)	1·81 (0·28)	9·46 (0·30)	11·20 (0·17)	42·30 (1·15)	30·31 (0·77)	—	26·44 (0·83)	0·95	—	7·22 (0·27)
P = 1·976 kbar, T = 811° C, fH_2[12] = 1 bar, 190 h																	
MP17 I	1·21 (S)	1·00	−11·78	1·83 (0·20)	2·0546	46·34	*−0·13 (0·15)*	*−0·96*	*9·08 (0·07)*	*8·25*	85·93 (3·31)	12·64 (1·65)	—	traces	1·88	—	0·47 (0·45)
MP17 II	2·24 (S)	1·00	−11·78	1·83 (0·20)	2·0525	46·17	*0·09 (0·20)*	*−0·96*	*9·30 (0·10)*	*8·25*	78·96 (3·06)	15·95 (1·54)	—	3·19 (1·68)	1·9	—	1·86 (0·42)
MP17 III	4·43 (S)	1·00 (0·01)	−11·79 (0·01)	1·83 (0·20)	2·0549	46·37	*−0·17 (0·16)*	*−1·10 (0·17)*	*9·04 (0·08)*	*8·11 (0·11)*	78·62 (3·61)	15·64 (1·85)	—	3·82 (1·92)	1·87	traces	4·40 (0·36)
MP17 IV	6·03 (S)	0·97 (0·04)	−11·82 (0·05)	1·80 (0·09)	2·0572	46·56	*−0·42 (0·15)*	*0·71 (0·98)*	*8·79 (0·08)*	*9·91 (0·30)*	78·50 (3·62)	15·70 (1·89)	—	3·82 (1·91)	1·87	traces	6·47 (0·48)
MP17 V	10·17 (S)	0·99 (0·01)	−11·79 (0·01)	1·82 (0·01)	2·0583	46·65	*−0·54 (0·16)*	*−0·39 (0·40)*	*8·67 (0·08)*	*8·82 (0·22)*	75·25 (3·43)	17·30 (1·78)	—	5·47 (1·83)	1·91	traces	9·78 (0·58)
MP17 VII[13]	3·80 (S)	1·00	−11·78	1·83 (0·20)	2·0547	46·35	*−0·14 (0·15)*	—	*9·06 (0·70)*	—	89·86 (0·57)	—	—	—	10·14	traces	—
MP17 VIII	1·10 (po5—po7)	1·00	−11·78	1·83 (0·20)	2·0652	47·25	*−1·41 (0·13)*	—	*7·80 (0·13)*	—	88·70 (1·37)	10·60 (1·11)	—	—	0·70 (0·16)	—	—
PIN17 VI	3·60 (S)	0·95 (0·05)	−11·83	1·79 (0·05)	—	—	—	1·06 (1·16)	—	10·27	43·62 (1·14)	28·96 (0·75)	—	26·46 (0·83)	0·96	—	5·87 (0·32)
P = 2·054 kbar, T = 930° C, fH_2[12] = 2·2 bar, 169 h																	
MP2 I	1·00 (S)	0·86	−9·99	1·39 (0·08)	2·0458	45·65	1·46	—	9·22	—	98·34 (0·56)	—	—	—	1·66	—	—
MP2 II	1·00 (po)	0·77	−10·09	1·29 (0·15)	2·0388	45·13	1·97	—	9·72	—	98·23 (0·56)	—	—	—	1·77	—	1·39 (0·65)
MP2 III	1·00 (an)	0·81	−10·04	1·34 (0·15)	—	—	—	—	—	—	96·07 (0·56)	—	—	—	1·50	2·43	—
P = 2·257 kbar, T = 933° C, fH_2[12] = 0·41 bar, 175 h																	
MP3 I	1·42 (S)	0·56	−8·90	2·42 (0·29)	—	—	—	—	—	—	98·10 (0·56)	—	—	—	traces	1·7	5·61 (0·06)
MP3 II	1·00 (po)	0·49	−9·02	2·30 (0·29)	—	—	—	—	—	—	99·13 (0·56)	—	—	—	—	0·87	4·56 (0·07)
MP3 III	1·00 (an)	0·99	−8·41	2·91 (0·29)	—	—	—	—	—	—	97·69 (0·56)	—	—	—	—	2·31	3·39 (0·08)
P = 1·986 kbar, T = 932° C, fH_2[12] = 4·67 bar, 175 h																	
MP4 I	1·03 (S)	0·62	−12·93	−1·58 (0·14)	2·0636	47·10	−0·21	—	7·51	—	98·33 (0·56)	—	—	—	1·67	—	1·95 (0·77)
MP4 II	1·00 (po)	0·43	−13·24	−1·89 (0·14)	2·0780	48·43	−2·26	—	5·48	—	97·12 (0·56)	—	—	—	2·88	—	2·33 (0·69)
MP4 III	1·00 (an)	0·78	−12·73	−1·38 (0·14)	2·0684	47·53	0·81	—	6·92	—	98·64 (0·56)	—	—	—	1·36	—	1·43 (0·58)

Charges	wt % S[1]	aH_2O[2]	$\log fO_2$[3]	ΔNNO[4]	d(102)[5]	at % Fe[6]	$\log fS_2$ (po)[7]	$\log fS_2$ (V)[8]	ΔFFS (po)[9]	ΔFFS (V)[10]	Gl	Pl	Px	Qz	Po	An	V
P = 2·116 kbar, T = 936° C, fH_2[12] = 0·9 bar, 164 h																	
MP9 I	1·07 (S)	0·96	−9·12	2·16 (0·13)	2·0606	46·85	0·16	—	7·98	—	99·22 (0·56)	—	—	—	0·78	traces	1·16 (0·65)
MP9 III	1·00 (po)	1·00	−9·01	2·27 (0·16)	2·0562	46·47	0·62	—	8·31	—	98·27 (0·56)	—	—	—	1·72	traces	—
MP9 V	1·00 (an)	1·00	−8·99	2·29 (0·16)	2·0567	47·10	−0·17	—	7·53	—	97·97 (0·56)	—	—	—	—	2·03	—
P = 2·013 kbar, T = 933° C, fH_2[11] = 47·3 bar, 166 h																	
MP10 I	2 (S)	0·81	−12·71 (0·12)	−1·38 (0·09)	2·0645	47·19	−0·31 (0·14)	−0·34	7·42 (0·07)	7·38 (0·22)	97·84	—	—	—	2·16	—	1·93 (0·45)
MP10 II	3 (S)	0·75	−12·78 (0·18)	−1·45 (0·13)	2·0585	46·67	0·35 (0·15)	*−1·21*(1·56)*	8·08 (0·07)	*7·60 (0·22)*	98·02	0·60 (0·74)	—	—	1·38	—	3·15 (0·61)
MP10 III	4 (S)	0·72	−12·82 (0·16)	−1·48 (0·11)	2·0572	46·55	0·49 (0·14)	−0·23 (0·61)	8·21 (0·07)	7·68 (0·16)	96·8	1·89 (0·80)	—	—	1·3	—	4·66 (0·53)
MP10 IV	10 (S)	0·5	−13·18 (0·37)	−1·85 (0·27)	2·0540	46·30	0·79 (0·14)	0·27 (0·48)	8·61 (0·07)	8·11 (0·14)	92·93	5·36 (1·04)	—	—	1·71	—	10·73 (0·96)
MP10 V	1 (po5)	1	−12·53 (0·14)	−1·18 (0·14)	2·0761	48·25	−1·93 (0·18)	—	5·79 (0·09)	—	96·16	—	—	—	3·85	—	—
MP10 VI	1 (po7)	1	−12·53 (0·14)	−1·18 (0·14)	2·0760	48·23	−1·91 (0·15)	—	5·82 (0·09)	—	96·55	—	—	—	3·45	—	—
P = 2·202 kbar, T = 935° C, fH_2[11] = 20·4 bar, 164 h																	
MP11 I	2·12 (S)	0·74	−11·96 (0·20)	−0·65 (0·14)	2·0553	46·40	0·70 (0·13)	−0·45 (2·18)	8·43 (0·07)	8·52 (0·22)	98·18	—	—	—	1·82	—	2·20 (0·79)
MP11 II	4·83 (S)	0·78	−11·92 (0·18)	−0·61 (0·13)	2·0512	46·13	1·01 (0·14)	*1·02*	8·73 (0·07)	*8·42 (0·24)*	98·96	—	—	—	1·04	—	2·95 (0·64)
MP11 III	4·83 (S)	0·63	−12·11 (0·19)	−0·80 (0·14)	2·0570	46·54	1·50 (0·14)	0·94 (0·42)	9·29 (0·07)	8·76 (0·13)	93·15	2·50 (1·36)	—	2·80 (1·51)	1·65	—	5·68 (0·65)
MP11 IV	10·12 (S)	0·51	−12·31 (0·37)	−1·00 (0·26)	n.d.			1·09 (0·50)	—	8·95 (0·15)	89·7	4·40 (1·33)	—	4·20 (1·50)	1·65	—	11·39 (0·95)
P = 2·202 kbar, T = 935° C, fH_2[11] = 20·4 bar, 164 h																	
MP11 V	1·20 (Po5)	0·97	−11·71 (0·05)	−0·41 (0·05)	2·0748	48·12	−1·68 (0·15)	—	6·05 (0·07)	—	96·9	—	—	—	3·1	—	—
MP11 VI	1·10 (Po7)	0·97	−11·71 (0·05)	−0·41 (0·05)	2·0750	48·15	−1·72 (0·16)	—	6·00 (0·08)	—	97·09	—	—	—	2·91	—	—
P = 2·003 kbar, T = 934° C, fH_2[11] = 15 bar, 213 h																	
MP6 II	0·62 (S)	0·83	−11·66 (0·20)	−0·34 (0·14)	2·0739	48·04	−1·57 (0·21)	—	6·15 (0·10)	—	99·13	—	—	—	0·87	—	—
MP6 III	1·02 (S)	0·74 (0·11)	−11·79 (0·18)	−0·46 (0·13)	2·0709	47·76	−1·14 (0·15)	*0·57 (0·92)*	6·58 (0·08)	*8·66 (0·20)*	98·34	—	—	—	1·66	—	1·43 (0·51)
MP6 IV	1·33 (S)	0·76 (0·15)	−11·76 (0·24)	−0·43 (0·17)	2·0631	47·06	−0·14 (0·14)	*1·25*	7·57 (0·07)	*8·62 (0·27)*	98·31	—	—	—	1·69	—	1·49 (0·68)
MP6VI	1·03 (Po7)	0·93	−11·56 (0·08)	−0·24 (0·08)	2·0740	48·05	−1·59 (0·15)	—	6·13 (0·07)	—	97·31	—	—	—	2·69	—	—
MP6VII	1·04 (Po5)	1	−11·50 (0·08)	−0·17 (0·08)	2·0740	48·05	−1·59 (0·15)	—	6·12 (0·08)	—	97·52	—	—	—	2·48	—	—
P = 2·092 kbar, T = 934° C, fH_2[11] = 6 bar, 147 h																	
MP12 I	2·31 (S)	0·77 (0·13)	−10·92 (0·21)	0·40 (0·15)	2·0541	46·30	*0·80 (0·14)*	1·97	*8·52 (0·07)*	9·35 (0·26)	97·85	—	—	—	2·15	—	1·67 (0·65)
MP12 II	3·90 (S)	0·79 (0·14)	−10·90 (0·21)	0·41 (0·15)	2·0552	46·39	0·70 (0·14)	1·96	8·42 (0·07)	9·33 (0·27)	97·89	—	—	—	2·11	—	4·04 (0·85)
MP12 III	5·86 (S)	0·65 (0·17)	−11·09 (0·33)	0·22 (0·23)	2·0569	46·53	0·53 (0·17)	2·23	8·25 (0·07)	9·65 (0·22)	91·85 (2·66)	3·60 (1·30)	—	3·00 (1·51)	1·65	—	6·23 (0·78)
MP12 IV	10·31 (S)	0·57 (0·18)	−11·22 (0·40)	0·10 (0·29)	2·0588	46·70	*0·33 (0·20)*	1·71	*8·06 (0·10)*	9·78 (0·19)	86·20 (2·75)	9·10 (1·34)	—	3·00 (1·56)	1·65	—	11·66 (0·88)
P = 1·980 kbar, T = 938° C, fH_2[11] = 4 bar, 162 h																	
MP7 III	1·00 (S)	0·78 (0·13)	−10·50 (0·21)	0·75 (0·15)	2·0443	45·53	*1·62 (0·12)*	2·16	*9·29 (0·06)*	9·46 (0·27)	98·61	—	—	—	1·39	—	1·40 (0·63)
MP7 IV	1·25 (S)	0·72 (0·08)	−10·56 (0·14)	0·69 (0·10)	2·0509	46·04	*1·10 (0·13)*	1·74 (0·60)	*8·76 (0·06)*	9·58 (0·16)	98·95	—	—	—	1·05	—	2·25 (0·43)
P = 2·001 kbar, T = 930° C, fH_2[11] = 0·8 bar, 168 h																	
MP13 I	2·00 (S)	0·38 (0·03)	−9·92 (0·06)	1·47 (0·05)	2·0530	46·21	0·86 (0·14)	2·75 (0·18)	8·62 (0·07)	10·52 (0·05)	96·21 (0·89)	—	—	—	1·63	0·37	3·80 (0·18)
MP13 II	3·87 (S)	0·36 (0·05)	−9·97 (0·15)	1·42 (0·11)	2·0577	46·60	*0·41 (0·14)*	2·79 (0·27)	*8·17 (0·07)*	10·59 (0·09)	95·74 (0·88)	—	—	2·13 (0·88)	1·69	0·43	5·80 (0·30)
MP13 III	6·04 (S)	0·29 (0·03)	−10·15 (0·13)	1·23 (0·09)	2·0538	46·28	*0·79 (0·16)*	3·00 (0·15)	*8·55 (0·08)*	10·77 (0·05)	97·41 (0·90)	—	—	traces	1·79 (0·85)	0·42	8·82 (0·63)
MP13 IV	10·11 (S)	0·22 (0·02)	−10·38 (0·13)	1·00 (0·09)	2·0554	46·41	*0·64 (0·22)*	3·16 (0·09)	*8·39 (0·11)*	10·92 (0·03)	98·03	traces	—	traces	1·73	0·24	13·37 (0·41)
P = 2·188 kbar, T = 894° C, fH_2[12] = 30 bar, 152 h																	
MP18 I	1·25 (S)	0·55 (0·09)	−11·64 (0·43)	−1·28 (0·43)	2·0737	48·02	−1·04 (0·16)	0·69 (1·12)	6·07 (0·08)	*8·30 (0·20)*	99·27	—	—	—	0·73	—	2·46 (0·13)
MP18 II	0·60 (S)	0·75 (0·05)	−11·29 (0·44)	−0·93 (0·44)	2·0734	47·99	−1·00 (0·22)	0·41 (0·98)	6·11 (0·11)	*7·94 (0·20)*	98·68	—	—	—	1·32	—	1·16 (0·20)
MP18 IV	2·04 (S)	0·65 (0·04)	−11·69 (0·52)	−1·34 (0·37)	2·0655	47·27	0·02 (0·14)	−0·10 (1·67)	7·13 (0·07)	7·89 (0·21)	98·42	—	—	—	1·58	—	2·72 (0·18)
MP18 V	4·32 (S)	0·37 (0·03)	−12·11 (0·42)	−1·75 (0·42)	2·0580	46·63	0·81 (0·13)	0·94 (0·78)	7·92 (0·06)	8·34 (0·18)	98·41	—	—	—	1·59	—	6·01 (0·20)
MP18 VI	6·33 (S)	0·23 (0·02)	−12·52 (0·42)	−2·15 (0·30)	2·0533	46·23	1·24 (0·12)	1·09 (0·77)	8·35 (0·06)	7·48 (0·18)	98·27	—	—	—	1·73	—	8·63 (0·15)

Table 4: continued

Charges	wt % S[1]	aH_2O[2]	$\log fO_2$[3]	ΔNNO[4]	d(102)[5]	at % Fe[6]	$\log fS_2$ (po)[7]	$\log fS_2$ (V)[8]	ΔFFS (po)[9]	ΔFFS (V)[10]	Gl	Pl	Px	Qz	Po	An	V
P = 2·188 kbar, T = 994°C, fH_2[12] = 30 bar, 152 h																	
MP18 VII	10·84 (S)	0·33 (0·03)	−12·21 (0·42)	−1·85 (0·30)	2·0509	46·04	1·44 (0·13)	0·99 (0·77)	8·55 (0·06)	8·38 (0·18)	98·17	–	–	–	1·83	–	12·73 (0·31)
MP18 X	3·62 (S)	0·56 (0·11)	−11·77 (0·40)	−1·41 (0·48)	2·0661	47·33	−0·05 (0·14)	0·63 (0·88)	7·06 (0·07)	8·09 (0·19)	98·45	–	–	–	1·55	–	6·52 (0·56)
MP18 XI	3·77 (S)	0·72 (0·15)	−11·55 (0·40)	−1·19 (0·48)	2·0727	47·93	−0·90 (0·15)	0·52 (0·52)	6·21 (0·07)	7·79 (0·28)	98·66	–	–		1·34	–	9·75 (0·62)
MP18 XII[13]	3·30 (S)	0·83 (0·07)	−11·11 (0·07)	−0·75 (0·07)	2·1718	47·84	−0·78 (0·14)	−1·36 (1·39)	6·33 (0·07)	8·23 (0·70)	97·24 (0·56)	–	–	–	2·76	–	2·54 (0·52)
MP18 SN	1·32 (pc6—pc7)	0·83	−11·1	−0·74	2·0741	48·06	−1·11 (0·11)	–	6·00 (0·12)	–	96·47	–	–	–	3·53*	–	–
PIN18 IX	3·26 (S)	0·24 (0·12)	−12·62 (0·64)	−2·26 (0·77)	2·0577	46·60	1·00 (0·13)	1·18 (0·62)	8·11 (0·06)	8·48 (0·27)	98·13 (0·56)	–	–	–	1·87	–	5·74 (0·63)
P = 2·058 kbar, T = 996°C, fH_2[12] = 2 bar, 162 h																	
MP19 VII	0·54 (S)	0·49 (0·11)	−9·26 (0·23)	1·06 (0·19)	–	–	–	2·22 (0·80)	–	9·59 (0·19)	100	–	–	–	–	–	2·09 (0·47)
MP19 II	1·42 (S)	0·75 (0·10)	−8·86 (0·16)	1·46 (0·12)	–	–	–	0·97 (0·97)	–	8·67 (0·25)	100	–	–	–	–	–	2·33 (0·46)
MP19 III	2·34 (S)	0·61 (0·16)	−9·08 (0·33)	1·25 (0·24)	–	–	–	1·31 (1·31)	–	9·34 (0·27)	99·34	–	–	–	0·66	–	3·57 (0·74)
MP19 IV	3·09 (S)	0·39 (0·17)	−9·52 (0·57)	0·81 (0·41)	–	–	–	1·55 (1·55)	–	9·86 (0·23)	99·39	–	–	–	0·61	–	5·33 (0·82)
MP19 VI	5·03 (S)	0·01	−12·61	−2·29	–	–	–	3·24	–	10·31	36·70	39	–	23	1·40	–	4·47 (0·10)
MP19 IX	3·39 (S)	0·88 (0·13)	−8·74 (0·18)	1·59 (0·12)	–	–	–	0·75 (0·57)	–	8·20 (0·31)	99·64	–	–	–	0·36	–	5·97 (0·60)
MP19 X	3·30 (S)	0·87 (0·13)	−8·74 (0·18)	1·59 (0·19)	–	–	–	0·78 (0·59)	–	8·25 (0·31)	100	–	–	–	traces	–	6·12 (1·12)
MP19 XI	3·29 (S)	0·88 (0·09)	−8·74 (0·12)	1·59 (0·09)	–	–	–	0·67 (0·50)	–	8·03 (0·29)	99·80	–	–	–	0·20	–	8·90 (0·47)
MP19 XII[13]	3·50 (S)	0·83 (0·17)	−8·80 (0·19)	1·53 (0·18)	–	–	–	−0·81 (2·65)	–	6·25 (1·32)	99·10 (0·56)	–	–	–	0·90	–	3·79 (0·80)
MP19 XIII	1·27 (pc6—pc7)	0·47	−9·27	1·05	–	–	–	2·48 (0·30)	–	9·55 (0·30)	98·29	–	–	–	1·71*	–	2·31 (0·78)
PIN19 VIII	3·15 (S)	0·41 (0·14)	−9·45 (0·45)	0·88 (0·32)	–	–	–	2·18 (1·21)	–	9·81 (0·21)	100	–	–	–	–	–	5·60 (0·66)
P = 1·992 kbar, T = 997°C, fH_2[12] = 0·5 bar, 157 h																	
MP14 I	1·99 (S)	0·47 (0·04)	−8·24 (0·12)	2·23 (0·09)	–	–	–	0·61 (0·49)	–	7·89 (0·14)	99·15 (0·92)	–	–	–	trace	0·85	3·99 (0·22)
MP14 II	3·86 (S)	0·43 (0·02)	−8·29 (0·07)	2·18 (0·06)	–	–	–	0·60 (0·29)	–	8·00 (0·09)	99·08	–	–	–	trace	0·92	6·00 (0·21)
MP14 III	6·04 (S)	0·31 (0·05)	−8·62 (0·19)	1·85 (0·14)	2·0529	46·20	*1·21 (0·17)*	1·42 (0·78)	*8·37 (0·08)*	8·85 (0·18)	97·90 (0·89)	–	–	–	1·08	1·02	8·31 (0·53)
MP14 IV	10·11 (S)	0·23 (0·03)	−8·86 (0·19)	2·00 (0·31)	2·0552	46·39	*1·01 (0·14)*	2·09 (0·37)	*8·17 (0·07)*	9·32 (0·12)	97·62	traces	–	–	1·38	1	12·09 (0·46)
MP14 VI	1·50 (pc6—pc7)	0·40 (0·05)	−8·38 (0·11)	2·03 (0·06)	2·0558	46·44	*0·95 (0·12)*	1·08 (0·30)	*8·11 (0·12)*	8·49 (0·30)	98·00 (1·25)	–	–	–	1·20 (0·22)	traces	3·45 (0·29)
MP14 VII[13]	3·50 (S)	0·57 (0·04)	−8·12 (0·02)	2·36 (0·03)	–	–	–	0·22 (0·19)	–	7·37 (0·09)	95·70 (0·59)	–	–	–	3·10	0·90	5·08 (0·22)
PIN14 VIII	3·78 (S)	0·43 (0·03)	−8·32 (0·08)	2·14 (0·06)	–	–	–	0·67 (0·32)	–	8·09 (0·10)	99·08 (0·91)	–	–	–	traces	traces	6·00 (0·21)

[1]Amount of sulphur added to the charge either as elemental (S) or as pyrrhotite (Po5—Po7; see Table 3).
[2]Water activity calculated from Burnham (1979).
[3]fO_2 computed from equation (2).
[4]fO_2 referenced to the NNO buffer (Holloway *et al.*, 1992).
[5]Distance between inter-reticular planes 102 of hexagonal pyrrhotite determined by XRD.
[6]Iron-content of pyrrhotite (atomic) from Yund & Hall (1976) using *d*(102).
[7]Log fS_2 given by the pyrrhotite composition, using the calibration of Froese & Gunter (1976). Numbers in italics are for $fO_2 >$ NNO (quenched Fe—S—O liquid).
[8]Log fS_2 calculated using and MRK-EOS (see text). Numbers in italics are for charges whose total sulphur content computed from MRK-EOS calculation is significantly different from the sulphur content calculated from mass balance.
[9]Log fS_2 calculated from pyrrhotite composition referenced to the iron–troilite (FFS) buffer (see text).
[10]Log fS_2 given by the MRK-EOS referenced to the iron–troilite (FFS) buffer (see text).
[11]fH_2 from membrane reading.
[12]fH_2 from NiPd sensor measurement.
[13]Magnetite-added charges.
Modal composition determined by mass balance. Phase abbreviations: Gl, glass; Pl, plagioclase; Px, pyroxene; Qz, quartz; Po, pyrrhotite; An, anhydrite; V, fluid phase. 1σ for Gl, Po, An, which are not given in parentheses, are 0·56, 0·16 and 0·13, respectively.

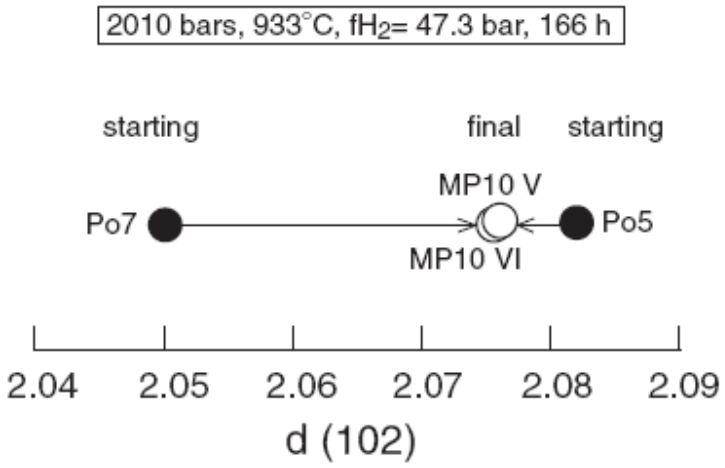

Fig. 2. Attainment of equilibrium in fS_2 for the experiment MP10. d(102) is the inter-reticular distance of the 102 plane of hexagonal pyrrhotite determined by XRD. Error bars are smaller than symbols. The starting pyrrhotite compositions (Po5 and Po7) are shown as black dots. Open dots are the final pyrrhotite compositions. The arrows indicate the changes in pyrrhotite compositions. Each pyrrhotite was loaded in separate capsules run at the same P–T–fH_2 conditions and the compositional similarity [similar d(102)] observed after the experiment indicates that both pyrrhotites record the same fS_2.

ANALYTICAL TECHNIQUES

Run products were examined by optical and scanning electron microscopy (SEM). We used X-ray diffractometry to confirm the phase assemblage determined by optical microscopy and SEM. Besides the characterization of the run products, X-ray diffractometry of powdered run products was also used to measure the composition of pyrrhotites (Arnold & Reicher, 1962; Toulmin & Barton, 1964; Boorman, 1967; Yund & Hall, 1969). Our measurements were made on an Inel CPS 120 diffractometer at ambient temperature using Co radiation (λ = 1.78897 A) with quartz as an external standard. The measured peak positions are accurate to within 0.01° (Roux & Volfinger, 1996).

Analyses of the major elements of the experimental charges were performed on both Camebax and SX50 electron microprobes. The operating analytical conditions were: accelerating voltage 15 kV, beam current 6 and 12 nA for glass and crystals, respectively, beam diameter 10 μm for glass and focused beam (1–2 μm) for crystals. A ZAF correction procedure was applied. Correction for electron beam induced alkali-migration and determination of H_2O concentration in glasses by the bydifference method (Devine et al., 1995) were performed by using calibration curves constructed from three hydrous standard glasses, analysed by wet chemistry for their Na and K content (Pichavant, 1987). These standards have the same composition as our starting material (without sulphur) and their water contents (up to 6.5wt%) are known from Karl Fisher titration. Major element calibration used wollastonite (Ca), hematite (Fe), albite (Na, Si), corundum (Al), olivine (Mg) and orthoclase (K) standards. The detection limit for major elements is about 1000 ppm. For the fH_2 sensor, the analytical conditions for Pt, Pd, Ni

were: accelerating voltage 20 kV and a focused beam current of 20 nA. Counting time was 10 s on the peak and 5 s on the background for all major element analyses. Anhydrite was analyzed (using a JEOL JXA-8600 electron microprobe) under analytical conditions of 15 kV, 6 nA and 5 μm beam diameter, using anhydrite as a standard.
The concentration of total sulphur in glasses was determined by electron microprobe analysis (Camebax). In silicate melts, sulphur is assumed to be present as sulphide (S^{2-}) or sulfate (S^{6+}) (Richardson & Withers, 1950; Ricke, 1960; Schneider, 1970). The position of the SKa X-ray has been shown to be a function of the sulphur valence state and of the complexation of sulphur (e.g. Carroll & Rutherford, 1988; Kucha et al., 1989). In our glasses, sulphur is present either as sulphide or sulfate, or as a mixture of the two. In this last case, the SKa X-ray peak is between the sulphide and sulfate positions. Therefore, at the beginning of each analytical session, we established two calibration curves—one for S as sulphide and one for S as sulfate. These curves were constructed with three synthetic hydrous dacitic standard glasses, containing 750, 1400, and 1900 ppm sulphur, determined by wet chemistry. The difference between the two calibration curves increases with the sulphur content, but remains below detection for S contents below 400 ppm. Consequently, the S-peak position was determined for all glasses with sulphur contents higher than 400 ppm, and the counting was performed on each specific peak. For S analyses, we used three PET crystal spectrometers, using the following analytical procedure: accelerating voltage 15 kV, sample current 50 nA, beam diameter 10 mm. Counting time was 60 s on each spectrometer, resulting in a total counting time of 180 s. The background was determined by analysing a glass of the same composition without sulphur, using the above analytical procedure. The detection limit under these analytical conditions is about 80 ppm, as calculated from Ancey et al. (1978). Single spot analyses of 1 h duration with these analytical conditions showed no migration of sulphur.
Qualitative analyses of oxygen in sulphides by electron microprobe (SX50) have been performed to check whether the pyrrhotites are the products of back reactions of immiscible Fe–S–O liquids upon quenching. Specifically, under conditions of high fO_2, pyrrhotite may partially break down to an Fe–O–S liquid. It appeared that, indeed, for fO_2 > NNO, most quench sulphides contained detectable amounts of oxygen. Therefore, the pyrrhotite in these charges may be because of the crystallization of Fe–S–O immiscible liquids during the quench, and we did not consider as reliable the fS_2 retrieved from pyrrhotite composition in those charges.

RESULTS

The experimental conditions, phase assemblages and proportions, and glass compositions are summarised in Tables 4 and 5.

Phase assemblages

The phase assemblages are portrayed in Fig. 3. Besides direct evidence of fluid in excess upon opening of the capsules, such as drops of water and hissing, fluid-saturated conditions were also assumed when bubble sizes in quenched glasses exceeded 10 mm. However, virtually all charges contain micrometric to sub-micrometric bubbles, which most probably represent remnants of air trapped in the capsules. No magnetite crystallized, except at high fO_2 (> NNO+1.3), where a trace amount of this oxide was detected (charges MP16 VII, MP17 VII and MP14 VII, Table 4). Previous experimental work, performed on various rhyolitic compositions, has shown that the

quench rates used in the present study are high enough to prevent quench crystallization of oxides (Gaillard et al., 2001). The comparison between magnetite-doped and undoped charges shows that below NNO+1, addition of magnetite to a sulphur-bearing charge merely results in extensive sulphide crystallization (Table 4). At all temperatures with fO_2 < NNO, the sulphide is pyrrhotite, whereas above NNO, the sulphide is an Fe–S–O immiscible liquid ± pyrrhotite, as indicated by detection of O by EMPA (Fig. 3). For charges in which the amount of added sulphur exceeds the sulphur solubility of the melt, an S–O–H fluid phase forms, and water becomes partitioned between melt and fluid. Further addition of sulphur to the system decreases the activity of water through a simple dilution effect (i.e. the H_2O/S ratio in the fluid decreases) and because of interaction with sulphur species (i.e. production of H_2S). A significant decrease in aH_2O may lead to the partial crystallization of other, S-free phases, such as plagioclase, pyroxene or quartz. For instance, at 800°C, plagioclase is stable for aH_2O slightly below 1, pyroxene is stable under reducing conditions for aH2O slightly below 1, and quartz crystallizes for aH_2O ≤0.85. Similarly, at 930°C, plagioclase is stable for aH_2O ≤0.75 and quartz is stable for aH_2O ≤0.65 above NNO-1. At 1000°C, apart from one charge which crystallized plagioclase, only S-bearing phases were present in charges loaded with elemental sulphur. Charges doped with magnetite resulted in extensive sulphide crystallization (up to 10 wt %), depending on the amount of sulphur added (Table 4), except at high fO_2 at 800 and 930°C, where iron oxides crystallized (MP16 VII, MP17 VII and MP14 VI charges, Table 4). Anhydrite is stable under oxidizing conditions only, confirming other experimental studies (Carroll & Rutherford, 1987; Luhr, 1990; Scaillet & Evans, 1999). At 800 and 930°C, anhydrite is stable at fO_2 > NNO+1. At 1000°C, anhydrite appears at fO_2 > NNO+1.8, which indicates that the fO_2 needed to crystallize anhydrite in rhyolitic melts increases with T (Fig. 3). Anhydrite stability in rhyolitic magmas appears to be in the same fO_2 range as that for trachyandesite magmas at T < 950°C (Carroll & Rutherford, 1987; Luhr, 1990).

Fluid phase composition

The composition of the coexisting fluid-phase was calculated using the MRK equation of state, as explained above. The mole fraction of H_2O in the fluid ($X_{H_2O_{fl}}$) ranges between near 1 and 0.1, yet, for the vast majority of charges, it is within the range 0.75–0.30. The few charges having $X_{H_2O_{fl}}$ significantly lower than 0.2 are those for which the by-difference method yields H_2O melt content close to zero (e.g. charge MP15V, Table 4). At all temperatures, as long as the fO_2 is below NNO+1, H_2S is the dominant sulphur-bearing species, and its mole fraction in the fluid ($X_{H_2S_{fl}}$ l) ranges from 0.1 up to 0.85. Thus, at 2 kbar and at an fO_2 below NNO+1, the fluid phase can be considered as a binary mixture of H_2O and H_2S, other fluid species (H_2, SO_2, S_2) amounting to no more than 0.01 mole fraction. SO_2 becomes abundant at higher fO_2 and its mole fraction ($X_{SO_{fl}}$) may even exceed that of H_2S at 930 and 1000°C. At 930°C, an fO_2 of NNO+1.4 is required to have $X_{SO_{fl}}$ > $X_{H_2S_{fl}}$. At 1000°C, the same happens at slightly lower fO_2, that is around NNO+1. At 800°C, however, H_2S dominates over SO_2, even with an fO_2 as high as NNO+1.8. At fO_2 > NNO+1, and in charges loaded with massive amounts of sulphur (5–10 wt %, Table 4), S_2 makes up a significant proportion of sulphur-bearing species in the fluid—up to 0.3 of $X_{S_{2fl}}$.

Table 5: Compositions of experimental glasses (normalized to 100 wt % anhydrous)

Charges	ΔNNO[1]	ΔFFS[2]	SiO_2	Al_2O_3	FeO[3]	MgO	CaO	Na_2O	K_2O	H_2O[4]	S (ppm)[5]	log S
P = 2·152 kbar, T = 785° C												
MP15 I	−1·12 (0·10)	7·45 (0·21)	78·35 (0·91)	13·25 (0·37)	0·28 (0·10)	0·29 (0·10)	1·62 (0·13)	4·17 (0·21)	2·02 (0·14)	4·69 (0·43)	≤D	—
MP15 II	−1·16 (0·29)	9·43 (0·19)	78·52 (0·99)	13·08 (0·41)	0·14 (0·10)	0·27 (0·10)	1·01 (0·11)	4·44 (0·24)	2·52 (0·18)	4·70 (1·00)	440 (11)	2·64
MP15 III	−1·83 (0·22)	9·95 (0·19)	78·63 (0·90)	12·54 (0·36)	0·14 (0·10)	0·26 (0·10)	0·94 (0·10)	4·18 (0·21)	3·30 (0·18	2·65 (0·44)	612 (19)	2·79
MP15 IV	−1·93 (0·39)	10·25 (0·18)	78·59 (0·65)	12·57 (0·26)	0·18 (0·10)	0·18 (0·10)	0·67 (0·10)	3·92 (0·15)	3·88 (0·14)	2·56 (0·70)	753 (40)	2·88
MP15 VI[6]	−0·93	6·19 (0·13)	78·03 (0·65)	13·02 (0·26)	1·51 (0·10)	0·17 (0·10)	1·65 (0·10)	3·71 (0·14)	1·89 (0·10)	5·54 (0·75)	≤D	—
MP15 VII[7]	−0·93	6·36 (0·22)	76·57 (1·27)	12·98 (0·52)	1·59 (0·18)	0·28 (0·10)	2·08 (0·21)	4·44 (0·32)	2·07 (0·23)	6·78 (0·65)	≤D	—
MP15 X	−1·03 (0·08)	7·42 (0·21)	77·53 (0·65)	13·71 (0·27)	0·17 (0·10)	0·32 (0·10)	1·98 (0·10)	4·34 (0·15)	1·94 (0·10)	5·93 (1·06)	126 (34)	2·10
MP15 XI	−0·98 (0·09)	7·13 (0·21)	77·46 (1·01)	13·75 (0·42)	0·63 (0·11)	0·35 (0·10)	2·00 (0·16)	3·87 (0·23)	1·93 (0·16)	6·37 (1·10)	≤D	—
MP15 SN	−1·18 (0·20)	7·24 (0·21)	77·96 (0·58)	13·51 (0·24)	0·23 (0·10)	0·34 (0·10)	1·77 (0·10)	4·27 (0·14)	1·92 (0·10)	4·60 (0·60)	96 (61)	1·98
PIN15VIII	−1·16 (0·07)	9·86 (0·19)	77·84 (1·17)	12·79 (0·47)	0·09 (0·10)	0·29 (0·10)	0·57 (0·10)	4·03 (0·28)	4·38 (0·29)	4·70 (0·30)	787 (21)	2·90
P = 1·973 kbar, T = 798° C												
MP16 I	1·30 (0·12)	10·76 (0·19)	78·78 (0·83)	12·31 (0·33)	0·16 (0·10)	0·33 (0·10)	1·45 (0·11)	2·87 (0·17)	4·10 (0·19)	5·01 (0·75)	108 (64)	2·03
MP16 II	1·18 (0·13)	10·99 (0·26)	78·83 (1·06)	12·20 (0·42)	0·08 (0·10)	0·33 (0·10)	1·04 (0·12)	2·79 (0·21)	4·71 (0·26)	4·32 (0·52)	294 (9)	2·47
MP16 III	1·16 (0·19)	11·04 (0·24)	78·10 (0·49)	12·16 (0·19)	0·10 (0·10)	0·36 (0·10)	0·99 (0·10)	3·02 (0·10)	5·27 (0·13)	4·31 (0·52)	240 (72)	2·38
MP16 IV	0·98 (0·13)	11·35 (0·11)	77·28 (0·74)	12·50 (0·30)	0·10 (0·10)	0·34 (0·10)	0·65 (0·10)	3·02 (0·15)	6·16 (0·21)	3·71 (0·41)	356 (22)	2·55
MP16 V	1·07 (0·16)	11·35 (0·08)	78·09 (0·57)	12·28 (0·22)	0·10 (0·10)	0·37 (0·10)	0·85 (0·10)	2·98 (0·11)	5·39 (0·15)	3·97 (0·54)	274 (16)	2·44
MP16 VII[7]	1·29	10·38 (0·46)	74·36 (0·49)	12·67 (0·20)	0·26 (0·10)	0·28 (0·10)	1·88 (0·10)	6·93 (0·15)	3·60 (0·11)	4·84 (0·41)	≤D	—
MP16VIII	1·41 (0·09)	10·06 (0·30)	78·04 (0·50)	12·47 (0·20)	0·58 (0·10)	0·29 (0·10)	1·67 (0·10)	2·96 (0·10)	3·97 (0·11)	5·71 (0·52)	≤D	—
MP16 IX	1·41 (0·02)	10·08 (0·27)	77·27 (0·39)	13·62 (0·16)	0·33 (0·10)	0·33 (0·10)	2·01 (0·10)	3·12 (0·10)	3·76 (0·10)	5·58 (0·34)	≤D	—
PIN16 VI	1·08 (0·13)	11·20 (0·17)	77·01 (0·52)	12·53 (0·21)	0·10 (0·10)	O.23 (0·10)	0·73 (0·10)	2·51 (0·10)	6·89 (0·15)	4·04 (0·47)	373 (14)	2·57
P = 1·976 kbar, T = 811° C												
MP17 I	1·83 (0·20)	—	80·01 (0·73)	12·06 (0·30)	0·10 (0·10)	0·37 (0·10)	1·41 (0·12)	3·89 (0·10)	2·15 (0·12)	5·88 (0·39)	125 (16)	2·1
MP17 II	1·83 (0·20)	—	79·93 (0·83)	12·13 (0·14)	0·08 (0·10)	0·40 (0·10)	1·21 (0·11)	3·93 (0·19)	2·32 (0·10)	5·86 (0·39)	263 (11)	2·42
MP17 III	1·83 (0·20)	—	79·90 (0·39)	12·17 (0·12)	0·11 (0·12)	0·40 (0·10)	1·12 (0·10)	3·98 (0·10)	2·32 (0·10)	5·49 (0·20)	304 (19)	2·48
MP17 IV	1·80 (0·09)	—	79·91 (0·70)	12·23 (0·26)	0·12 (0·10)	0·40 (0·10)	1·06 (0·10)	3·94 (0·15)	2·33 (0·18)	5·46 (0·43)	279 (18)	2·45
MP17 V	1·82 (0·01)	—	79·96 (0·70)	12·21 (0·22)	0·06 (0·10)	0·42 (0·10)	1·04 (0·16)	3·87 (0·21)	2·44 (0·17)	5·62 (0·38)	307 (11)	2·49
MP17 VII[7]	1·83 (0·20)	—	77·84 (0·81)	13·42 (0·41)	0·40 (0·43)	0·31 (0·10)	1·99 (0·15)	4·19 (0·18)	1·95 (0·10)	6·21 (0·47)	83 (24)	1·92
MP17 VIII[6]	1·83 (0·20)	—	78·62 (1·33)	12·48 (0·24)	1·39 (0·27)	0·21 (0·10)	1·51 (0·10)	3·67 (0·41)	2·12 (0·23)	6·74 (1·25)	≤D	—
PIN 17 VI	1·79 (0·05)	—	79·05 (0·70)	13·04 (0·20)	0·11 (0·14)	0·22 (0·10)	1·05 (0·10)	3·30 (0·13)	3·22 (0·11)	5·43 (0·56)	281 (11)	2·45
P = 2·054 kbar, T = 930° C												
MP2 I	1·39 (0·08)	9·22	76·92 (0·10)	13·62 (0·10)	0·48 (0·10)	0·35 (0·10)	2·07 (0·10)	4·57 (0·10)	1·99 (0·10)	4·97 (0·37)	158 (12)	2·20
MP2 II	1·29 (0·15)	9·72	75·83 (0·23)	13·34 (0·10)	2·41 (0·10)	0·33 (0·1à)	1·95 (0·10)	4·22 (0·10)	1·92 (0·10)	4·44 (0·59)	112 (13)	2·05
MP2 III	1·34 (0·15)	—	77·25 (0·33)	13·55 (0·14)	0·45 (0·10)	0·35 (0·10)	2·01 (0·10)	4·43 (0·10)	1·94 (0·10)	4·71 (0·79)	285 (15)	2·46

Charges	ΔNNO[1]	ΔFFS[2]	SiO_2	Al_2O_3	FeO[3]	MgO	CaO	Na_2O	K_2O	H_2O[4]	S (ppm)[5]	log S
P = *2·257 kbar*, T = *933°C*												
MP3 I	2·42 (0·29)	—	77·30 (0·23)	13·73 (0·10)	1·85 (0·10)	0·32 (0·10)	0·39 (0·10)	4·40 (0·10)	2·01 (0·10)	3·04 (0·47)	989 (19)	2·99
MP3 II	2·30 (0·29)	—	76·90 (0·32)	13·50 (0·13)	1·81 (0·10)	0·33 (0·10)	1·18 (0·10)	4·37 (0·10)	1·90 (0·10)	2·83 (0·70)	307 (14)	2·49
MP3 III	2·91 (0·29)	—	76·22 (0·30)	13·40 (0·13)	1·93 (0·10)	0·33 (0·10)	2·10 (0·10)	4·05 (0·10)	1·96 (0·10)	4·89 (0·60	186 (13)	2·27
P = *1·986 kbar*, T = *932°C*												
MP4 I	−1·58 (0·14)	7·51	77·19 (0·10)	13·66 (0·23)	0·19 (0·10)	0·32 (0·10)	2·04 (0·10)	4·60 (0·13)	1·99 (0·10)	3·72 (0·72)	313 (13)	2·50
MP4 II	−1·89 (0·14)	5·46	76·31 (0·26)	13·59 (0·11)	1·43 (0·10)	0·34 (0·10)	2·02 (0·10)	4·38 (0·10)	1·93 (0·10)	2·81 (0·65)	≤D	—
MP4 III	−1·38 (0·14)	6·92	75·55 (0·22)	13·38 (0·10)	0·43 (0·10)	0·20 (0·10)	4·23 (0·10)	4·28 (0·10)	1·93 (0·10)	4·37 (0·53)	148 (11)	2·17
P = *2·116 kbar*, T = *936°C*												
MP9 I	2·16 (0·13)	7·86	76·85 (0·66)	13·54 (0·31)	1·16 (0·16)	0·32 (0·10)	2·02 (0·10)	3·99 (0·12)	2·12 (0·10)	4·74 (0·58)	77 (61)	1·89
MP9 III	2·27 (0·16)	8·31	76·08 (0·77)	13·53 (0·28)	2·40 (0·27)	0·34 (0·10)	1·91 (0·10)	3·70 (0·59)	2·03 (0·10)	5·13 (0·56)	≤D	—
MP9 V	2·29 (0·16)	7·53	75·81 (0·63)	13·24 (0·34)	1·87 (0·17)	0·35 (0·10)	2·64 (0·10)	3·98 (0·17)	2·11 (0·10)	5·76 (0·49)	154 (6)	2·19
P = *2·013 kbar*, T = *933°C*												
MP10 I	−1·38 (0·09)	7·42 (0·07)	77·34 (0·67)	13·52 (0·22)	0·31 (0·17)	0·30 (0·10)	2·04 (0·10)	4·38 (0·12)	2·10 (0·10)	4·51 (0·36)	189 (36)	2·28
MP10 II	−1·45 (0·13)	8·08 (0·07)	77·42 (0·61)	13·60 (0·25)	0·13 (0·25)	0·32 (0·10)	1·99 (0·10)	1·39 (0·14)	2·15 (0·10)	4·25 (0·48)	544 (20)	2·74
MP10 III	−1·48 (0·11)	8·21 (0·07)	77·71 (0·38)	13·35 (0·16)	0·20 (0·16)	0·32 (0·10)	1·95 (0·10)	4·38 (0·10)	2·08 (0·10)	4·09 (0·40)	691 (76)	2·84
MP10 IV	−1·85 (0·27)	8·51 (0·07)	77·08 (1·72)	12·94 (0·73)	0·12 (0·16)	0·33 (0·10)	1·70 (0·18)	5·55 (1·39)	2·26 (0·10)	3·14 (0·67)	883 (33)	2·95
MP10 V[6]	−1·18 (0·14)	5·79 (0·09)	76·76 (0·76)	13·37 (0·23)	1·35 (0·22)	0·31 (0·10)	1·99 (0·10)	4·15 (0·15)	2·07 (0·10)	5·90 (0·55)	≤D	—
MP10 VI[6]	−1·18 (0·14)	5·82 (0·09)	76·81 (0·77)	13·35 (0·25)	1·22 (0·25)	0·32 (0·10)	1·99 (0·10)	4·26 (0·15)	2·04 (0·10)	5·54 (0·52)	≤D	—
P = *2·202 kbar*, T = *935°C*												
MP11 I	−0·65 (0·14)	8·43 (0·07)	77·31 (0·67)	13·40 (0·29)	0·34 (0·25)	0·32 (0·10)	2·04 (0·10)	4·48 (0·14)	2·11 (0·10)	4·39 (0·55)	211 (52)	2·32
MP11 II	−0·61 (0·13)	8·73 (0·07)	77·44 (0·70)	13·55 (0·20)	0·05 (0·10)	0·33 (0·10)	2·08 (0·10)	4·48 (0·12)	2·07 (0·11)	4·56 (0·54)	644 (31)	2·81
MP11 III	−0·80 (0·14)	9·29 (0·07)	77·27 (0·66)	13·60 (0·22)	0·11 (0·14)	0·32 (0·10)	2·05 (0·10)	4·52 (0·10)	2·12 (0·10)	3·86 (0·46)	718 (44)	2·86
MP11 IV	−1·00 (0·26)	8·95 (0·15)	77·39 (0·80)	13·54 (0·28)	0·09 (0·10)	0·35 (0·10)	1·92 (0·10)	4·50 (0·22)	2·21 (0·10)	3·31 (0·71)	901 (22)	2·95
MP11 V[6]	−0·41 (0·05)	6·05 (0·07)	76·38 (0·68)	13·16 (0·24)	1·86 (0·21)	0·33 (0·10)	2·01 (0·14)	4·17 (0·26)	2·08 (0·10)	5·36 (0·37)	≤D	—
MP11VI[6]	−0·41 (0·05)	6·00 (0·08)	76·40 (0·50)	13·38 (0·27)	1·54 (0·17)	0·31 (0·10)	2·01 (0·10)	4·24 (0·19)	2·11 (0·11)	5·38 (0·30)	≤D	—
P = *2·003 kbar*, T = *934°C*												
MP6 II	−0·34 (0·14)	6·15 (0·10)	76·79 (1·10)	13·67 (0·27)	1·06 (0·56)	0·35 (0·10)	1·97 (0·10)	3·99 (0·15)	2·16 (0·10)	4·50 (0·57)	72 (62)	1·86
MP6 III	−0·46 (0·13)	6·58 (0·08)	77·34 (0·51)	13·77 (0·25)	0·44 (0·22)	0·35 (0·10)	2·00 (0·10)	4·02 (0·18)	2·08 (0·10)	4·07 (0·46)	74 (62)	1·87
MP6 IV	−0·43 (0·13)	7·57 (0·07)	77·33 (0·68)	13·67 (0·22)	0·43 (0·27)	0·34 (0·10)	1·98 (0·11)	4·13 (0·15)	2·11 (0·13)	4·21 (0·29)	≤D	—
MP6 VI[6]	−0·24 (0·08)	6·13 (0·07)	76·49 (0·83)	13·55 (0·16)	1·62 (0·21)	0·31 (0·10)	2·06 (0·11)	3·88 (0·18)	2·08 (0·10)	4·86 (0·79)	≤D	—
MP6 VII[6]	−0·17 (0·08)	6·12 (0·08)	76·03 (0·59)	13·51 (0·24)	2·11 (0·23)	0·33 (0·10)	1·97 (0·10)	3·94 (0·10)	2·10 (0·10)	5·38 (0·45)	≤D	—

Charges	ΔNNO[1]	ΔFFS[2]	SiO_2	Al_2O_3	FeO[3]	MgO	CaO	Na_2O	K_2O	H_2O[4]	S (ppm)[5]	log S
P = *2·092 kbar*, T = *934° C*												
MP12 I	0·40 (0·15)	9·35 (0·26)	77·43 (0·65)	13·53 (0·24)	0·09 (0·10)	0·34 (0·10)	2·01 (0·10)	4·45 (0·11)	2·13 (0·10)	4·43 (0·59)	273 (38)	1·58
MP12 II	0·41 (0·15)	9·33 (0·27)	77·33 (0·83)	13·62 (0·20)	0·12 (0·12)	0·33 (0·10)	2·05 (0·12)	4·39 (0·16)	2·15 (0·10)	4·48 (0·62)	334 (77)	2·52
MP12 III	0·22 (0·23)	9·65 (0·22)	77·60 (1·17)	13·48 (0·31)	0·11 (0·10)	0·33 (0·10)	1·94 (0·10)	4·35 (0·23)	2·18 (0·13)	3·83 (0·77)	535 (47)	2·73
MP12 IV	0·10 (0·29)	9·78 (0·19)	78·77 (1·03)	12·75 (0·43)	0·07 (0·12)	0·32 (0·10)	1·47 (0·14)	4·36 (0·23)	2·25 (0·10)	3·47 (0·82)	554 (43)	2·74
P = *1·980 kbar*, T = *938° C*												
MP7 III	0·75 (0·15)	9·46 (0·27)	76·98 (0·54)	13·79 (0·19)	0·69 (0·14)	0·32 (0·10)	2·04 (0·10)	4·08 (0·11)	2·08 (0·10)	4·27 (0·57)	≤D	—
MP7 IV	0·69 (0·10)	9·58 (0·16)	76·90 (0·74)	13·60 (0·20)	0·94 (0·59)	0·36 (0·10)	2·03 (0·10)	4·06 (0·15)	2·11 (0·10)	4·02 (0·36)	≤D	—
P = *2·001 kbar*, T = *930° C*												
MP13 I	1·47 (0·05)	10·52 (0·05)	77·31 (0·44)	13·94 (0·19)	0·38 (0·10)	0·31 (0·10)	1·79 (0·10)	4·39 (0·11)	1·88 (0·10)	2·51 (0·11)	371 (51)	2·57
MP13 II	1·42 (0·11)	10·59 (0·09)	77·21 (0·76)	13·97 (0·32)	0·31 (0·10)	0·30 (0·10)	1·72 (0·11)	4·63 (0·19)	1·86 (0·12)	2·45 (0·19)	422 (25)	2·63
MP13 III	1·23 (0·09)	10·77 (0·05)	77·75 (0·54)	13·75 (0·23)	0·21 (0·10)	0·33 (0·10)	1·70 (0·10)	4·38 (0·13)	1·87 (0·10)	2·10 (0·13)	494 (86)	2·69
MP13 IV	1·00 (0·09)	10·92 (0·03)	77·19 (0·44)	13·87 (0·19)	0·29 (0·10)	0·38 (0·10)	1·89 (0·10)	4·53 (0·11)	1·85 (0·10)	1·83 (0·10)	429 (31)	2·63
P = *2·188 kbar*, T = *994° C*												
MP18 I	−1·28 (0·43)	6·07 (0·08)	77·32 (0·40)	13·73 (0·17)	0·46 (0·10)	0·34 (0·10)	2·02 (0·10)	4·23 (0·10)	1·89 (0·10)	3·37 (0·12)	284 (47)	2·45
MP18 II	−0·93 (0·44)	6·11 (0·11)	77·08 (0·59)	13·68 (0·25)	0·92 (0·10)	0·32 (0·10)	2·07 (0·10)	4·12 (0·14)	1·80 (0·10)	4·24 (0·19)	147 (29)	2·17
MP18 IV	−1·34 (0·37)	7·13 (0·07)	77·51 (0·49)	13·69 (0·21)	0·26 (0·10)	0·33 (0·10)	2·07 (0·10)	4·26 (0·12)	1·87 (0·10)	3·82 (0·15)	453 (98)	2·66
MP18 V	−1·75 (0·42)	7·92 (0·06)	77·22 (0·59)	13·80 (0·25)	0·16 (0·10)	0·31 (0·10)	2·10 (0·10)	4·53 (0·14)	1·88 (0·0)	2·62 (0·15)	660 (38)	2·82
MP18 VI	−2·15 (0·30)	8·35 (0·06)	77·31 (0·46)	13·78 (0·20)	0·09 (0·10)	0·34 (0·10)	2·12 (0·10)	4·52 (0·11)	1·83 (0·10)	1·92 (0·10)	907 (41)	2·96
MP18 VII	−1·85 (0·30)	8·55 (0·06)	77·52 (0·58)	13·64 (0·24)	0·12 (0·10)	0·31 (0·10)	2·09 (0·10)	4·46 (0·14)	1·85 (0·10)	2·34 (0·14)	1154 (21)	3·06
MP18 XII	−0·75 (0·07)	6·33 (0·07)	76·70 (0·51)	13·67 (0·22)	1·09 (0·10)	0·33 (0·10)	2·07 (0·10)	4·24 (0·12)	1·90 (0·10)	4·82 (0·49)	178 (57)	2·25
MP18 SN[6]	−0·74	6·00 (0·12)	76·33 (0·44)	13·72 (0·19)	1·50 (0·10)	0·32 (0·10)	2·03 (0·10)	4·20 (0·10)	1·90 (0·10)	4·47 (0·61)	116 (23)	2·06
PIN18 IX	−2·26 (0·77)	8·11 (0·06)	77·00 (0·77)	13·51 (0·32)	0·27 (0·10)	0·33 (0·10)	2·09 (0·13)	4·89 (0·19)	1·90 (0·12)	1·80 (0·54)	698 (64)	2·84
P = *2·068 kbar*, T = *996° C*												
MP19 VII	1·06 (0·19)	9·59 (0·19)	75·98 (0·48)	13·43 (0·20)	1·94 (0·10)	0·33 (0·10)	2·07 (0·10)	4·36 (0·12)	1·89 (0·10)	3·01 (0·46)	≤D	—
MP19 II	1·46 (0·12)	8·67 (0·25)	76·06 (0·49)	13·41 (0·20)	2·11 (0·10)	0·33 (0·10)	2·11 (0·10)	4·13 (0·11)	1·85 (0·10)	4·17 (0·43)	≤D	—
MP19 III	1·25 (0·24)	9·34 (0·27)	76·36 (0·51)	13·54 (0·22)	1·46 (0·10)	0·35 (0·10)	2·08 (0·10)	4·28 (0·12)	1·91 (0·10)	3·57 (0·71)	132 (70)	2·12
MP19 IV	0·81 (0·41)	9·86 (0·23)	76·23 (0·68)	13·54 (0·29)	1·50 (0·10)	0·32 (0·10)	2·15 (0·11)	4·33 (0·16)	1·93 (0·11)	2·61 (0·77)	≤D	—
MP19 VI	−2·29	10·31	77·44 (0·88)	11·79 (0·34)	1·13 (0·11)	0·39 (0·10)	0·91 (0·10)	3·17 (0·18)	5·17 (0·23)	0·25 (0·25)	≤D	—
MP19 IX	1·59 (0·12)	8·20 (0·31)	76·91 (0·53)	13·83 (0·22)	1·71 (0·10)	0·33 (0·10)	2·08 (0·10)	3·28 (0·11)	1·85 (0·10)	4·53 (0·52)	≤D	—
MP19 X	1·59 (0·19)	8·25 (0·31)	76·28 (0·80)	13·47 (0·33)	2·09 (0·13)	0·35 (0·10)	2·14 (0·13)	3·74 (0·18)	1·92 (0·13)	5·15 (1·08)	122 (70)	2·09
MP19 XI	1·59 (0·09)	8·03 (0·29)	76·40 (0·50)	13·57 (0·21)	1·84 (0·10)	0·33 (0·10)	2·06 (0·10)	3·90 (0·11)	1·89 (0·10)	4·65 (0·37)	145 (21)	2·16
MP19 XII	1·53 (0·18)	6·25 (1·23)	75·36 (0·48)	13·44 (0·20)	3·06 (0·10)	0·32 (0·10)	2·03 (0·10)	3·85 (0·11)	1·93 (0·10)	4·44 (0·73)	167 (23)	2·22
MP19 XIII[6]	1·05	9·55 (0·30)	74·93 (0·48)	13·49 (0·21)	3·40 (0·11)	0·32 (0·10)	1·97 (0·10)	4·04 (0·11)	1·85 (0·10)	2·84 (0·79)	≤D	—
PIN19 VIII	0·88 (0·32)	9·81 (0·21)	78·32 (0·62)	12·99 (0·25)	0·80 (0·10)	0·25 (0·10)	1·29 (0·10)	3·49 (0·13)	2·85 (0·12)	2·60 (0·61)	≤D	—

Table 5: continued

Charges	ΔNNO[1]	ΔFFS[2]	SiO_2	Al_2O_3	FeO[3]	MgO	CaO	Na_2O	K_2O	H_2O[4]	S (ppm)[5]	log S
P = *1·992 kbar*, T = *987°C*												
MP14 I	2·23 (0·09)	7·89 (0·14)	76·71 (0·66)	13·67 (0·28)	2·20 (0·12)	0·34 (0·10)	1·30 (0·10)	3·93 (0·15)	1·84 (0·10)	2·80 (0·18)	674 (104)	2·83
MP14 II	2·18 (0·06)	8·00 (0·09)	76·88 (0·44)	13·73 (0·18)	2·13 (0·10)	0·32 (0·10)	1·24 (0·10)	3·90 (0·10)	1·79 (0·10)	2·67 (0·11)	563 (77)	2·75
MP14 III	1·85 (0·14)	8·85 (0·18)	77·60 (0·83)	13·90 (0·35)	0·92 (0·11)	0·35 (0·10)	1·15 (0·10)	4·16 (0·19)	1·92 (0·13)	2·11 (0·20)	734 (49)	2·87
MP14 IV	2·00 (0·31)	9·32 (0·12)	77·60 (0·45)	14·02 (0·19)	0·63 (0·10)	0·33 (0·10)	1·18 (0·10)	4·34 (0·11)	1·89 (0·10)	1·78 (0·10)	771 (31)	2·89
MP14 VI[6]	2·03 (0·06)	8·49 (0·30)	75·88 (0·77)	13·35 (0·32)	3·17 (0·16)	0·30 (0·10)	1·62 (0·11)	3·88 (0·18)	1·79 (0·12)	2·53 (0·20)	399 (88)	2·60
MP14 VII	2·36 (0·03)	10·88 (0·09)	76·08 (0·58)	13·48 (0·24)	3·26 (0·12)	0·31 (0·10)	1·15 (0·10)	3·90 (0·13)	1·81 (0·10)	3·19 (0·16)	645 (75)	2·64
PIN14 VIII	2·14 (0·06)	—	78·66 (0·48)	12·99 (0·19)	0·89 (0·10)	0·23 (0·10)	1·19 (0·10)	3·28 (0·10)	2·76 (0·10)	2·64 (0·12)	186 (14)	2·27

Numbers in parentheses indicate 1 standard deviation of replicate analyses.
[1]fO_2 normalized to the NNO buffer (see Table 4).
[2]fS_2 normalized to the FFS buffer (see Table 4).
[3]Total Fe, given as FeO.
[4]Water content determined using the by-difference method.
[5]Total sulphur content. D is the detection limit (80 ppm).
[6]Pyrrhotite-added charges.
[7]Magnetite-added charges.

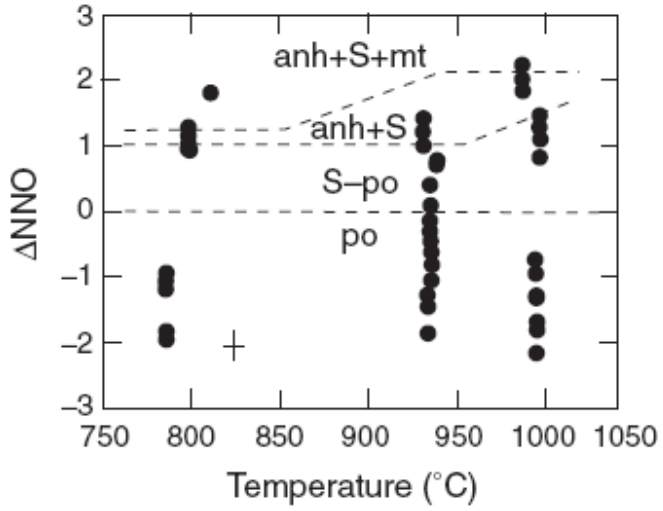

Fig. 3. Stability domains of sulphur-bearing phases as a function of fO_2 and temperature. Phase abbreviations: anh, anhydrite; po, pyrrhotite; S, immiscible Fe–S–O liquid; mt, magnetite.

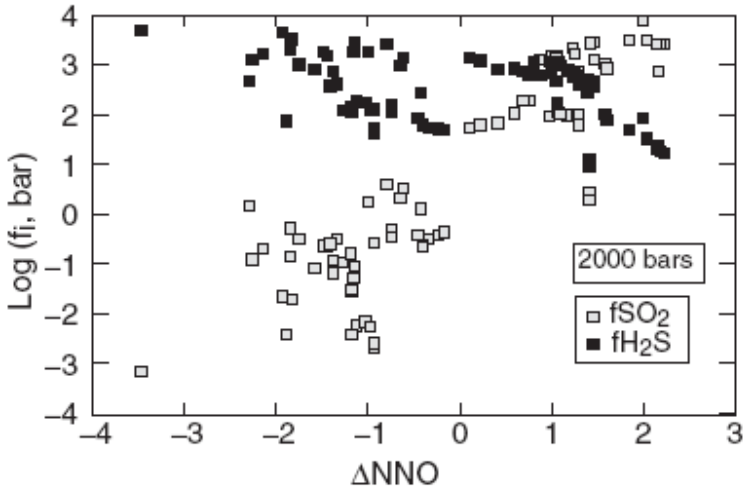

Fig. 4. Fugacities of H_2S and SO_2 fluid species versus the corresponding fO_2 for all charges for which fS_2 could be determined, calculated using equations (7) and (8) (see Table 4 and text). The increase in fO_2 favours SO_2 relative to H_2S species in the fluid phase. At any given fO_2, the spread in either fH_2S or fSO_2 reflects the variations in fS_2 that are a result of the varying amounts of sulphur loaded to the charge.

Figure 4 shows the calculated fugacities of both H_2S and SO_2 species in the fluid for all charges for which fS_2 is available, plotted against the corresponding fO_2. The fugacity of H_2S (fH_2S) ranges from 10 to 4.977 kbar, whereas that of SO_2 (fSO_2) covers a wider range, from 10^{-4} to 7.804 kbar. The crossover between f H_2S and fSO_2 occurs at around

NNO+1. In fact, it is only at fO_2 > NNO+2 and at 930 and 1000°C that fSO_2 is several orders of magnitude larger than f H_2S.

Major element glass composition

Glasses obtained using the Pinatubo composition, which is richer in alkalis than that from Mt Pelee (Table 1), display similar sulphur concentrations when held under similar fO_2 and fS_2, except at high fO_2, where Pinatubo charges are slightly richer in sulphur than the Mt Pelee ones. Overall, however, because Pinatubo charges do not depart significantly from the trends defined by the Mt Pelee ones, in the following, both groups are considered together. The glasses are rhyolitic, with SiO2 contents predominantly in the range 76–78 wt % and Al_2O_3 = 13 $\pm$ 1 wt %. Variations in the concentrations of other elements affect primarily Fe and Ca, as both elements are removed by either sulphide or sulfate crystallization. In addition, at 930 and 800°C, the crystallization of plagioclase, quartz and pyroxene also affects the melt chemistry, most notably its CaO and K_2O concentrations (Tables 4 and 5). In particular, at 800°C, a continuous increase in K_2O arises as a result of the dominantly incompatible behaviour of this element (see MP16 series, Table 5). At all values of fS_2, fO_2 and T, a broad negative correlation can be established between FeO and melt sulphur content in sulphide-bearing charges (Fig. 5). All glasses to which elemental sulphur was added and which were held at fO_2 < NNO+1 are depleted to various extents in iron compared with the starting composition (2 wt % FeO), because of crystallization of sulphide (Fig. 5). In contrast, most charges with sulphur added as pyrrhotite have glasses richer in iron than other charges run under the same T, fO_2 but loaded with elemental sulphur (see Table 5). Charges doped with magnetite also display higher iron contents than undoped ones held at the same T and fO_2. It is important to note that most glasses with low to very low iron contents display the highest sulphur contents, whereas those with the highest iron content have the lowest sulphur content, often below the detection limit (Fig. 5). Glasses of charges held at an fO_2 > NNO+1 display consistently higher iron contents than all other charges having similar amounts of dissolved sulphur (Fig. 5)—an effect of the crystallization of anhydrite in lieu of pyrrhotite at high fO_2.

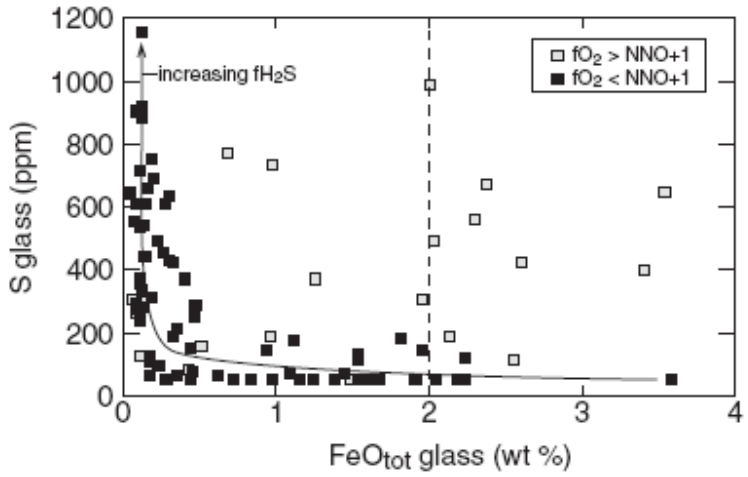

Fig. 5. FeO_{tot} vs melt-sulphur content of experimental glasses at all investigated temperatures for reduced and oxidized conditions. The latter correspond in general to anhydrite-bearing charges. Note the general leftward displacement relative to the starting composition (dashed line at 2 wt %) of most charges. The arrow indicates that, below NNO+1, the general increase in melt-sulphur content is a result of the increase in fH_2S (and temperature).

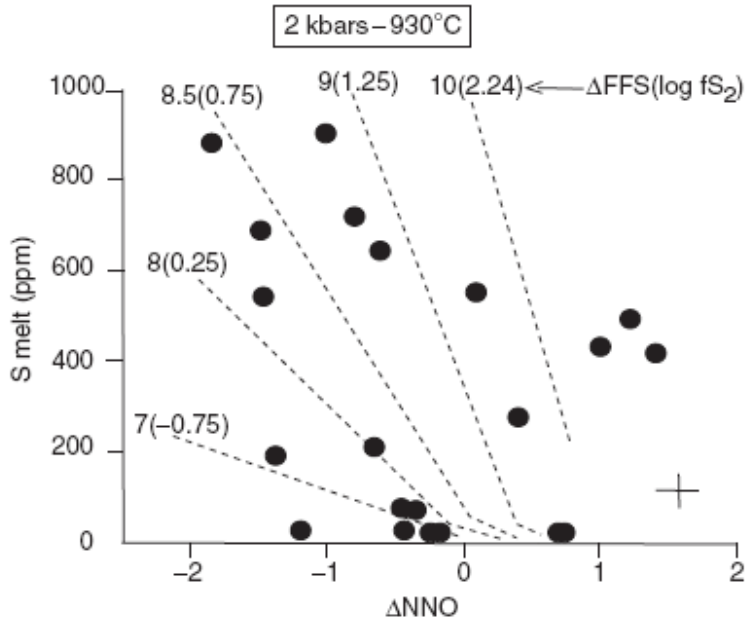

Fig. 6. Sulphur concentration in glass as a function of fO_2 and fS_2 at 930°C. Dotted lines are contours of iso-fS_2, labelled with ΔFFS in bold and corresponding fS_2 in parentheses.

Solubility of sulphur as a function of intensive parameters

The interrelationships between melt sulphur content, fS_2 and fO_2 at 930°C, where most of the data were obtained, are shown in Fig. 6. The solubility of sulphur is clearly a function of both fO_2 and fS_2. Below NNO+1, for a fixed fO_2, the solubility of sulphur

increases with fS_2. Above NNO+1, the data are scarce but suggest the same trend of increasing sulphur content with increasing fS_2. For any given fS_2, the sulphur solubility decreases when fO_2 increases, so as to reach a minimum between NNO and NNO+1. The data suggest that this minimum in sulphur solubility moves towards more oxidizing conditions when fS_2 increases. The relationships between melt sulphur concentration (Smelt), fS_2, fH_2S, fSO_2 for various fO_2 and at the three investigated temperatures are shown in Fig. 7. There is a general systematic increase in Smelt with fS_2, most clearly seen at low fO_2 (< NNO + 1). As a rule, an increase in fO_2 leads to a decrease in Smelt at fixed fS_2. This effect is most apparent at 800 and 930°C. Exceptions to this behaviour concern experiments performed at 930 and 1000°C in the fO_2 range NNO+0.7 to NNO+1, where the Smelt content displays few variations, being close to the detection limit (Fig. 7). No clear trend appears when using fSO_2 in place of f S_2 (Fig. 7), even under high fO_2, where SO_2 is the dominant sulphur-bearing species in the fluid. In contrast, Smelt correlates strongly with fH_2S. At 800°C, the two data groups at NNO-1.4 and NNO+1.2 merge into a single, well-defined trend, whereas using fS_2 leads to two distinct series. Similarly, at 930°C, a general single positive correlation emerges, with much less dispersion than when fS_2 is used as a variable. At 1000°C, a strong positive correlation is clearly defined only for an fO_2 of NNO-1.4. At all temperatures, Smelt exceeds 200 ppm once f H_2S is above a few hundred bars. At NNO-1.4, when the mole fraction of S (X_S, calculated using common rock-forming oxides such as SiO_2, Al_2O_3, etc.) is used in place of concentration (Smelt), the correlations defined with f H_2S appear to be linear at all temperatures (Fig. 8). Under high fO_2, a broad positive correlation exists between X_S and fSO_2, but with significant scatter and no apparent temperature effect can be resolved, unlike at low fO_2. The scatter is because of the difficulties in precisely determining fS_2 under high fO_2 conditions.

Sulphur speciation in hydrous rhyolite melt

Since the pioneering work of Fincham & Richardson (1954), it is common to envision sulphur dissolution in anhydrous silicate melts either as sulphide (low-fO_2) or as sulphate (high-fO_2) species, depending on prevailing redox state, through the following two reactions (see Carroll & Webster, 1994) :

$$\tfrac{1}{2}S_2 + O^{2-} \Leftrightarrow \tfrac{1}{2}O_2 + S^{2-}$$

$$\tfrac{1}{2}S_2 + \tfrac{3}{2}O_2 + O^{2-} \Leftrightarrow SO_4^{2-}$$

where S^{2-} and $SO^{2\ 4-}$ refer respectively to sulphide and sulphate species dissolved in the melt and O^{2-} represents oxygen anions in the silicate melt. A quantitative assessment of reactions (12) and (13) has been so far limited by our inhability to rigorously evaluate the proportion, as well as the activity–composition relationships, of O^{2-} in complex hydrous alumino-silicate melts such as magmatic liquids. The strong correlation existing between Fe and Smelt in both natural and experimental anhydrous glasses suggests that S^{2-} exchanges preferentially with O^{2-} bound to ferrous iron in melts under low fO2, whereas at high fO_2, anhydrite precipitation suggests that the exchange primarily takes place with

oxygens associated to Ca. In hydrous melts, the same reactions are supposed to operate (Carroll & Webster, 1994). In particular, under low fO_2, sulphur dissolution might happen through a reaction such as (Carroll & Webster, 1994)

$$H_2S_{gas} + FeO_{melt} \Leftrightarrow FeS_{melt} + H_2O_{gas}.$$

This reaction predicts that sulphur solubility in ironbearing hydrous melt should increase with the activity of FeO, which is contrary to what our experimental data show (Fig. 5). However, based on experimental as well as on energetic and volumetric considerations, in particular the similarity of H_2O and H_2S molecules, Burnham (1979) proposed that sulphur dissolution into iron-poor hydrous rhyolitic melts is analogous to the H_2O solution reaction, and can be described by the following reaction :

$$H_2O_{gas} + SH^-_{melt} \Leftrightarrow H_2S_{gas} + OH^-_{melt}.$$

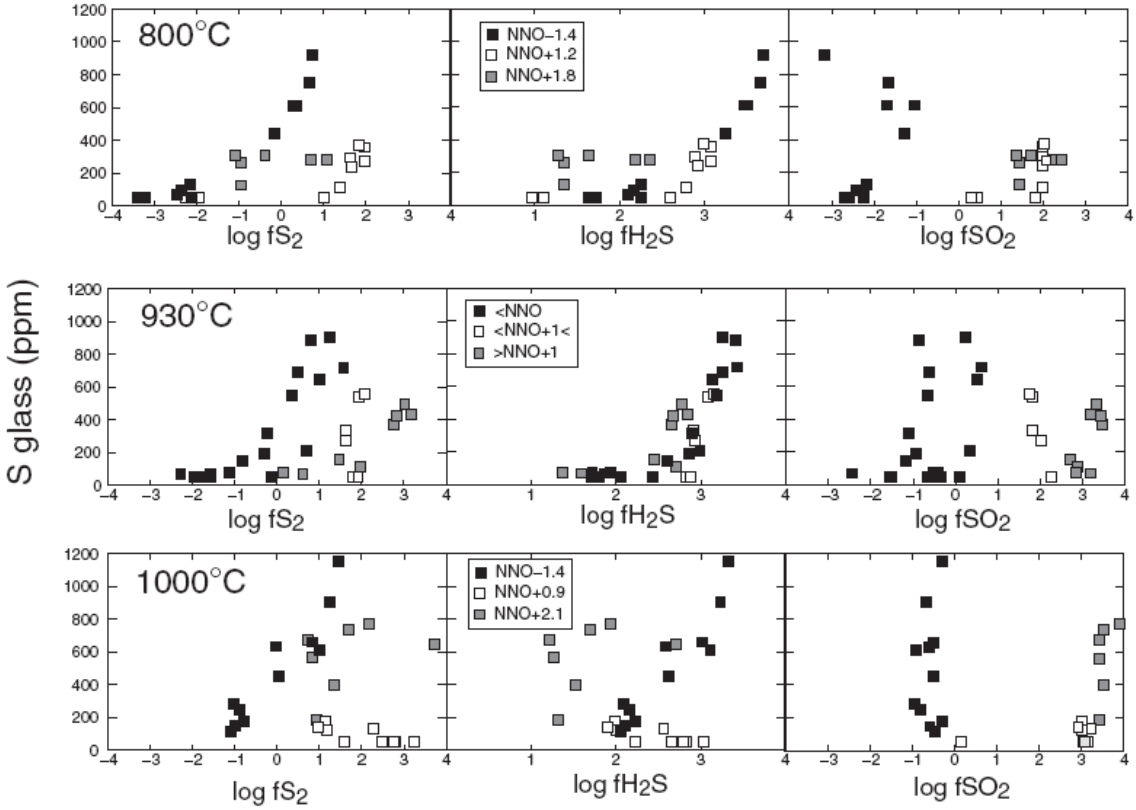

Fig. 7. Relationships between melt-sulphur concentration (Smelt), and f S_2, fH_2S, fSO_2 for various fO_2, at the three investigated temperatures. For clarity at 930°C, the data have been grouped into three fO_2 intervals, each broadly corresponding to a different type of S-bearing phase (as fO_2 increases: pyrrhotite, occurrence of an immiscible Fe–S–O liquid, and anhydrite).

Burnham (1979) reported a sulphur solubility of 1700 ppm at 2 kbar, 850°C in a hydrous, pyrrhotite saturated, rhyolitic melt (initial iron content of 0.3 wt %). This sulphur concentration is higher than the maxima attained in our study, and, upon completion of the run, it was found that, essentially, all the iron initially present in the system is fixed in pyrrhotite (Burnham, 1979)—an observation that corroborates our findings at low fO_2. The very fact that similar, or even higher, sulphur concentrations compared with those achieved in the present work have been reported in either H_2O bearing (Keppler, 1999) or H2O-free (Mysen & Popp, 1980) haplogranite or albite melts (i.e. melts without iron) shows that iron is not instrumental in achieving high sulphur concentration in silicate melts. That, first, a negative correlation exists between dissolved iron and sulphur (Fig. 5), secondly, the glasses having the highest sulphur concentration are also those having the lowest iron content, close to the detection limit and, thirdly, a strong positive correlation exists between f H_2S and Smelt all suggest that reactions such as (15) may better account for our experimental observations, at least those below NNO+1, rather than reactions in which iron-bearing species are involved. Under oxidizing conditions, the situation is less clear but sulphur dissolution in hydrous melts may occur via the following reaction :

$$\mathrm{SO_2 + 2OH^- \Leftrightarrow SO_4^{2-} + H_2.}$$

Unfortunately, a rigorous evaluation of reactions (14)–(16) is hampered primarily by the lack of knowledge about the nature of sulphur species dissolved in silicate melts, as well as of the activity–composition relationships of melt components, and these are clearly two main avenues for future research on the behaviour of sulphur in silicate melts.

Thermodynamic model of sulphur solubility in hydrous and iron-poor rhyolite melts

In this section, in the absence of specific speciation data and on the basis that H_2S and SO_2 are the major sulphurbearing species in the coexisting fluid phase, we assume that the total dissolved sulphur in the melt results from the addition of sulphur dissolved from H_2S and SO_2 dissolution reactions. The extent of each dissolution reaction is controlled by the magnitude of both H_2S and SO_2 fugacities in the system. We thus have

$$X_{\mathrm{S}} = X_{\mathrm{reduced}} + X_{\mathrm{oxidized}}$$

where $X_{reduced}$ and $X_{oxidized}$ represent the mole fractions of sulphur species dissolved under the reduced and oxidized forms, hereafter referred to as $X_{H2Smelt}$ and $X_{SO2melt}$, respectively. Regardless of the actual sulphur species in the melt, the data allow us to evaluate the standard thermodynamic parameters of the following heterogeneous reactions between fluid and melt (e.g. Spera & Bergman, 1980) :

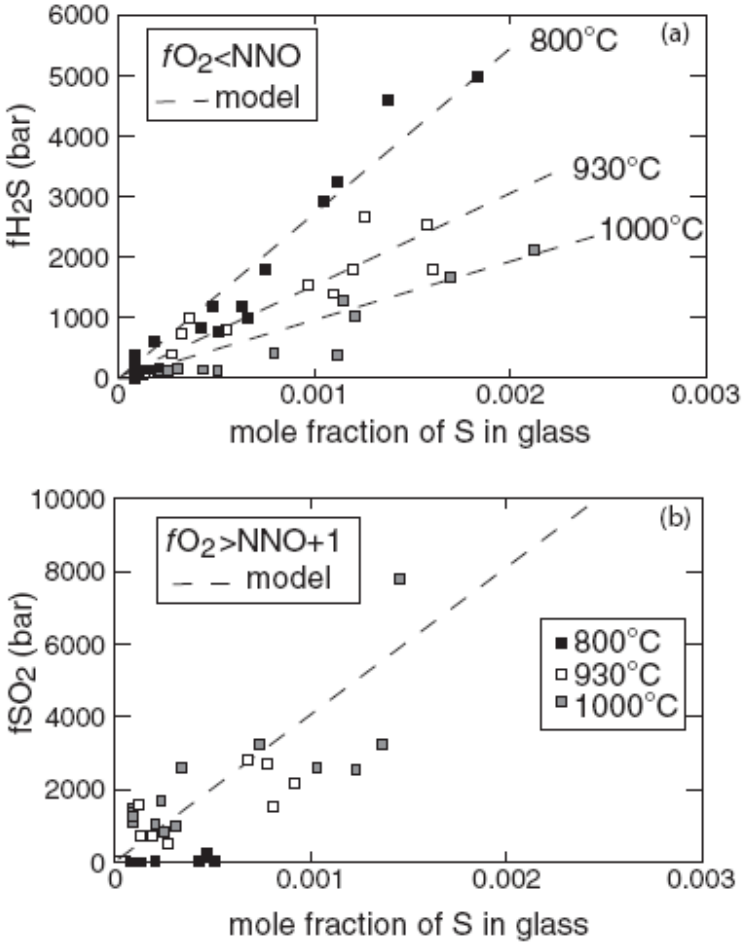

Fig. 8. Xi–fi relationships. (a) Under reduced conditions (ΔNNO ≤ 0), where the dominant S-bearing species in the fluid is H_2S. (b) Under oxidizing conditions (ΔNNO ≥ 1.0), where the dominant S-bearing species in the fluid is SO_2. Dashed curves are sulphur solubilities calculated using the thermodynamic model developed in the text.

$$H_2S_{melt} \Leftrightarrow H_2S_{fluid}$$

and

$$SO_{2melt} \Leftrightarrow SO_{2fluid}$$

whose equilibrium constants are

$$K_{18} = f\mathrm{H_2S_{fluid}} / a_{\mathrm{H2Smelt}}$$

And

$$K_{19} = f\mathrm{SO_{2fluid}} / a_{\mathrm{SO2melt}}.$$

Assuming that $a_i = X_i$, then

$$K_{18} = f\mathrm{H_2S_{fluid}} / X_{\mathrm{H2Smelt}}$$

And

$$K_{19} = f\mathrm{SO_{2fluid}} / X_{\mathrm{SO2melt}}.$$

To evaluate the above reactions, we proceed by considering separately charges at fO_2 < NNO, in which H_2S is the dominant sulphur-bearing species in the fluid, and then charges at fO_2 > NNO+1.5, in which SO_2 is the dominant sulphur-bearing species. Under those conditions, the right-hand side of equation (17) simplifies to either $X_{H2Smelt}$ (fO_2 < NNO) or $X_{SO2melt}$ (fO_2 > NNO+1.5).

H_2S dissolution

At all temperatures and $fO_2 \leq$ NNO, the relationships between X_S and f H_2S is within error linear (Fig. 8) and, thus, the solubility of H_2S in rhyolite melt obeys Henry's Law, i.e. at fixed P and T,

$$f\mathrm{H_2S} = X_{\mathrm{H2Smelt}}\, k_{\mathrm{H}}$$

where k_H is the Henry's Law constant and is obviously equivalent to K_{18}. As shown in Fig. 8, the f H_2S–$X_{H2Smelt}$ relationships display well organized trends with temperature. Departure from the simple Henrian behaviour, because of both temperature and pressure variations, can be accounted for by using the following classical equation (e.g. Fogel & Rutherford, 1990) :

$$\ln(f\mathrm{H_2S}/X_{\mathrm{H2Smelt}}) = \ln k_{\mathrm{H(Pr,Tr)}} + (\Delta H/R)(1/T - 1/T_{\mathrm{r}}) + (V_{\mathrm{H2S}}(P - P_{\mathrm{r}}))/RT \qquad (21)$$

which, upon rearrangement, gives

$$X_{\mathrm{H2Smelt}} = f\mathrm{H_2S}/k_{\mathrm{H\,(Pr,Tr)}} \exp[-(\Delta H/R)(1/T - 1/T_{\mathrm{r}}) - (V_{\mathrm{H2S}}(P - P_{\mathrm{r}}))/RT] \quad (22)$$

in which T_r and P_r are the reference temperature and pressure, respectively, ΔH is the heat of H_2S dissolution into the melt, R is the gas constant and V_{H2S} the partial molar volume of H_2S melt species. T_r and P_r were, respectively, chosen to be 930°C, as most of the data were gathered along or close to this isotherm, and 0 bar. Equation (22) has been extensively used in the thermodynamic modelling of H_2O and CO_2 solubilities in various silicate–melt compositions (e.g. Stolper et al., 1987; Fogel & Rutherford, 1990; Blank et al., 1993). Non-linear least-squares regression using charges with an $fO_2 \leq$ NNO-1.4 gives the following values: $k_{H,930°C}$ = 0.801 10^6 bar, ΔH = 54.85 kJ/mol and V_{H2S} = 26.03 cm^3/mol. The Henry constant is similar to that found for CO_2 dissolution in rhyolite melt (1.106 10^6 bar, Fogel & Rutherford, 1990). However, contrary to both H_2O and CO_2 species, the enthalpy of H_2S solution is positive in sign, which simply means that, at a given fH_2S, temperature increases the solubility of sulphur. Although the partial molar volume of H_2S in rhyolite melt appears to be similar to that of H_2O, we stress that our data cover a range in f H_2S too small to allow extraction of volume properties with great accuracy. In fact, the investigated pressure domain falls in the range where sulphur exhibits essentially linear dependence on fH_2S, i.e. where V_{H2S} plays a negligible role in equation (22).

SO_2 dissolution

At fO_2 > NNO+1·5, because of the difficulties in retrieving fluid species fugacities in the oxidized range, the dispersion in the X_S–fSO_2 (Fig. 8) plot is much more severe than for H_2S, and it can only be assumed that sulphur dissolution at high fO_2 also follows Henry's Law. Linear regression of the data obtained at an fO_2 > NNO+1·5 gives the following value for the Henry constant: $K_{SO2} = K_{19}$ = 4·13 x 10^6 bar.

Sources of error

The calculated versus measured sulphur mole fractions for various fH_2S are shown in Fig. 9 for charges held at an fO_2 of NNO–1·4 or lower.

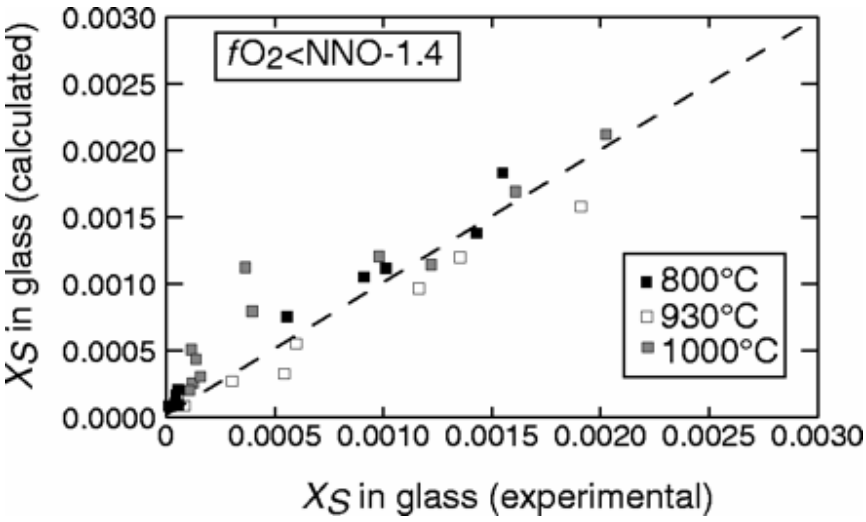

Fig. 9**.** Experimental versus calculated mole fractions of sulphur for charges at an fO_2 of below NNO–1·4, using the thermodynamic model developed in the text.

Although the model correctly reproduces the measured values, there is a substantial scatter around the 1:1 correlation line. Besides the obvious fact that not all dissolved sulphur needs to be in the H_2S form, one major source of error that affects the derivation of thermodynamic parameters comes from the calculated values of fH_2S. In experimental studies designed to calibrate H_2O or CO_2 solubility models, the fluid species fugacities are calculated from equations of state in which uncertainties in fugacities essentially come from uncertainties in P and T measurements. Here, the H_2S fugacities are also affected by this source of uncertainty, but also by (1) the analytical uncertainty attached to the determination of pyrrhotite composition and (2) the lack of well-calibrated EOS for sulphur-bearing volatile species. The analytical uncertainty in measured fS_2 is typically 0·2 log units (Table 3). Taking charge MP15V as an example, its measured fS_2 is 5·46 bar (log fS_2 = 0·74), to which corresponds an fH_2S of 4·977 kbar, given the fH_2 of 27 bar. If, instead, fS_2 is 8·66 bar (log fS_2 = 0·94), then the calculated fH_2S would be 6·265 kbar or *c*. 25% higher absolute. There is thus no doubt that the thermodynamic quantities derived above need to be confirmed, in particular by designing specific experimental procedures to achieve equilibration of rhyolite melts with pure H_2S fluid (or SO_2) and by exploring the behaviour at higher fH_2S and fSO_2 than those attained in the present study to constrain more rigorously the partial molar volumes of H_2S and SO_2-related species (see below also). The data suggest, however, that, under low fO_2 and in iron-poor silicate melts, H_2S dissolution may occur through formation of HS-like complexes, and that at high fO_2, SO_2 reacts with OH^- groups to yield SO_4^{2-}. Clearly, however, there is a need for more direct information (spectroscopic) about potential S complexes present in silicate melts (e.g. Winther *et al*., 1998), as the common peak-shift method is unable to distinguish between S^2-associated with Fe^{2+} from those linked to H^+ cations.

Solubility minimum and speciation

Despite these caveats, the thermodynamic properties derived above for H_2S and SO_2 dissolution in hydrous rhyolite melt can be combined to compute the behaviour of total dissolved sulphur, X_S (= $X_{H2Smelt}$ + $X_{SO2melt}$, as defined above in equations (18)–(22)) under various T and fO_2 conditions. An Excel spreadsheet, which calculates the fugacities of S_2, H_2S, SO_2 and H_2O, species at fixed P, T, S_{melt} and fO_2, using the thermodynamic approach detailed above, is available upon request from the second author. The results of such calculations are shown in Fig. 10a for 930°C, 2 kbar, several fS_2 within the fO_2 range NNO–2 to NNO+3. As shown in Fig. 10a, the model reproduces the classical inverted bell-shaped pattern of sulphur solubility with varying fO_2. At all fS_2, the minimum calculated centers at NNO+1, in good agreement with experimental observations in the present (Fig. 6) as well as in other studies (see Carroll & Webster, 1994).

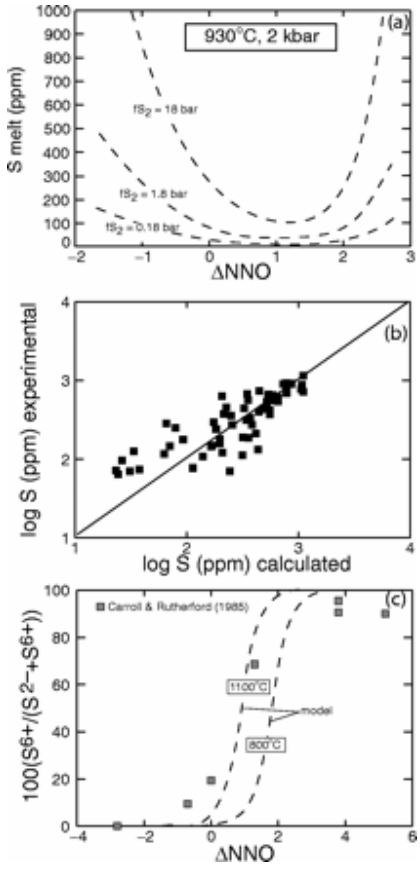

Fig. 10. Application of the thermodynamic model. (a) Calculated total dissolved sulphur (S_{ppm}) against fO_2 (ΔNNO) at 930°C and for an fS_2 of ΔFFS+7 (log fS_2 = –0·75), ΔFFS+8 (log fS_2 = 0·24), and ΔFFS+9 (log fS_2 = 1·24). All calculations have been performed with fH_2O = 1 kbar, which corresponds to a melt-water content of *c*. 4·5 wt %. (b) Comparison between observed and calculated melt sulphur contents for all charges in which fS_2 could be estimated. (c) Calculated proportions of S^{6+} at 1100 and 800°C, as a function of ΔNNO. The gray squares represent the experimental data of Carroll & Rutherford (1988).

It shows also that as fS_2 decreases, this bell-shaped pattern opens wide to the extent of becoming almost flat at very low values of fS_2. Specifically, at 930°C, any fS_2 lower than 0·17 bar (FFS+7) results in no apparent variations in sulphur concentrations with varying fO_2 (note that the curve still has a bell-shaped pattern, even at very low sulphur concentrations, but the concentration scale over which it occurs is well below the detection limit of EPMA). Conversely, an fS_2 of 18 bar (FFS+9) leads to a strongly asymmetrical and steep-sided shape of the sulphur concentration curve with varying fO_2. The calculated melt-sulphur concentrations for all charges for which fS_2 and fH_2 are available are plotted against those measured in Fig. 10b. The model reproduces well the experiments in the high concentration range, above 200 ppm, which reflects, in part, that the analytical accuracy is better at high concentration.

Given the above model assumptions, we can also calculate the proportions of S^{2-} and S^{6+} melt species, assuming that S^{2-} and S^{6+} abundances are fixed by H_2S and SO_2 dissolution reactions (18) and (19), respectively. Figure 10c shows the proportion of S^{6+} calculated for 1100 and 800°C isotherms. At a given P, T and fO_2, the fS_2 has no effect on species proportions. In contrast, temperature does affect the calculated proportions so that lower temperature increases the proportion of sulphide species at any fixed fO_2. As shown in Fig. 10c, the calculated pattern of species proportion broadly conforms with that obtained by Carroll & Rutherford (1988) from peak-shift measurements carried out on a series of synthetic sulphur-bearing glasses, annealed under various redox conditions in the temperature range 920–1150°C. The difference between model and observations may be a result of the fact that melt compositions synthesized by Carroll & Rutherford (1988) are less silicic than those of the present work.

Empirical model of sulphur solubility in rhyolite melts

The application of the thermodynamic model presented above requires the determination of both fH_2S and fSO_2. These two quantities are not usually measured on magmatic rocks, in contrast to both fO_2 and fS_2, which are more easily estimated from Fe–Ti oxides or sulfide barometry (Whitney, 1984). Although derivation of fSO_2 from fO_2 and fS_2 is straightforward, calculation of fH_2S requires fH_2 to be known in addition to fS_2 or, alternatively, the determination of fH_2O if fO_2 is known. This supplementary step introduces an additional source of uncertainty, that is, the determination of melt water content from which fH_2O is calculated. To overcome this potential problem and given the restricted compositional range displayed by the experimental glasses, we have derived an empirical model in which T, fO_2 and fS_2 are the only required input parameters: such a model is simpler in its application and, therefore, of more direct petrological use. Given that many arc magmas have fO_2 below NNO+1·5, we have restricted the fitting procedure to charges lying below this fO_2 threshold: this has the advantage that only the charges for which fS_2 is best known are taken into account. Considering the different effects of fO_2, fS_2 and T on the melt–sulphur content illustrated above, the experimental data were fitted by least-squares regression to the following equation, taking into account only glasses with sulphur-content higher than the detection limit:

$$\log \mathrm{S\,(ppm)} \;=\; 0.001T\,(^{\circ}C) \;-\; 0.2567\;\Delta\mathrm{NNO}$$
$$+\; 0.1713\Delta\mathrm{FFS} \;+\; 0.0034\;\Delta\mathrm{NNO} \times \Delta\mathrm{FFS}$$

or

$$\frac{\log \mathrm{S} \;-\; 0.001T \;+\; 0.2567\;\Delta\mathrm{NNO}}{0.1713 \;+\; 0.0034\Delta\mathrm{NNO}} \;=\; \Delta\mathrm{FFS}.$$

As with fO_2, referencing fS_2 to a standard solid buffer such as FFS removes the temperature dependence and improves the quality of the fit. Knowing the sulphur content of a glass, the temperature and fO_2 of the system, equation (24) allows calculation of fS_2.

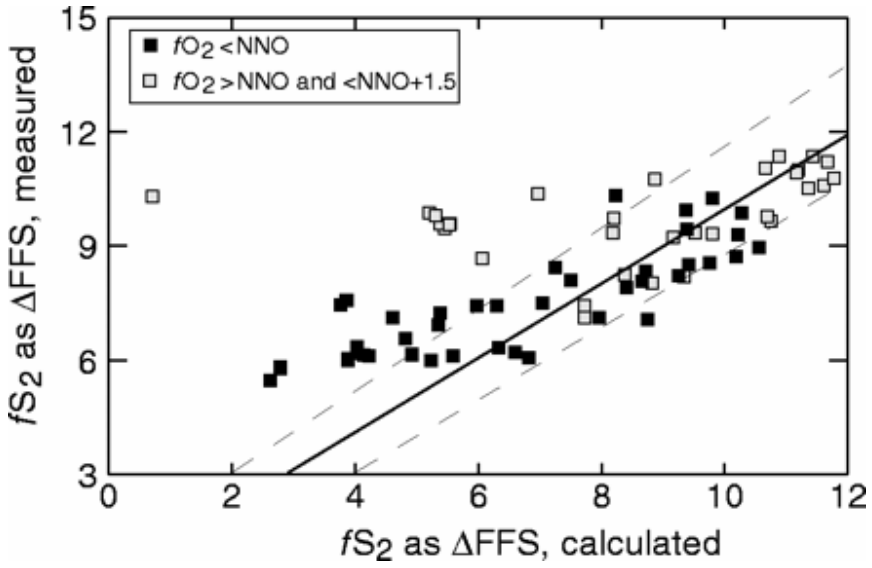

Fig. 11. Comparison between measured and calculated sulphur fugacities using the empirical model [equation (24)]. See text for explanation.

Figure 11 shows model performances for all charges held at an fO_2 < NNO+1·5. Equation (24) reproduces observed values to within 1 log units at ΔFFS > 6, apart from a few charges in the fO_2 range NNO to NNO+1·5. At lower ΔFFS, the model tends to underestimate fS_2—a reflection of the difficulty in measuring sulphur content in glasses in the low concentration range (<100 ppm). We stress that equation (24) is merely a convenient mathematical way to describe the interdependence between the various parameters that control the sulphur solubility in rhyolite melts at 2 kbar and it has no thermodynamic meaning.

DISCUSSION

Fluid and melt-sulphur relationships

The general coherency of the experimental trends obtained between intensive (fO_2, fS_2) and extensive (S in melt) parameters shows that the adopted experimental procedure has been successful in either accurately controlling fO_2 or measuring fS_2. The observed solubility trends can be interpreted in terms of different solubility behaviour of the different S-species present in the coexisting fluid. Because the fluid phase composition is sensitive to redox conditions, any change in fO_2 profoundly affects the sulphur solubility. The more soluble sulphur species appear to be H_2S and SO_2. The sulphur behaviour in hydrous silicate melts can thus be modelled using a simple thermodynamic approach, similar to that employed for characterizing the solubilities of both H_2O and CO_2 volatiles in silicate melts, considering the additive effects of two basic dissolution reactions involving either H_2S or SO_2 fluid species. At fixed *P* and *T*, Henry's Law is obeyed for H_2S and possibly SO_2 species, up to fugacities of 5 and 8 kbar, respectively. At equal fugacities, H_2S appears to be more soluble than SO_2, and, hence, the asymmetrical behaviour of sulphur on both sides of the solubility minimum. This asymmetry is also a result of the differing *PVT* properties of H_2S and SO_2 fluid species. The MRK model predicts that SO_2 exhibits a more pronounced non-ideal behaviour than H_2S (that is higher fugacity coefficients), and thus the fugacities of either end-member (i.e. pure SO_2 or H_2S fluids at any fixed *P* and *T*) and their mixing behaviour will also control the shape of the solubility curve. In other words, even if both H_2S and SO_2 were to have identical Henry's Law constants, because the fugacities of pure H_2S or SO_2 differ at fixed *P* and *T*, this will ultimately impart an asymmetrical shape on the solubility curve with changing redox conditions. In this regard, it would be of interest to constrain the solubility of silicate melts with respect to H_2S and SO_2 by performing experiments with pure H_2S and SO_2 fluids. The minimum in solubility appears to lie in the redox range where H_2S and SO_2 fugacities in the fluid are approximately equal (Fig. 4), and MRK calculations show that S_2 is comparatively more abundant in this domain. This latter species is thus apparently weakly soluble in silicate melts and plays a minor role in the melt-sulphur budget.

The effect of iron

The experimental procedure adopted here does not allow independent variation of fS_2 and the melt-FeO content (Fig. 5). In particular, at any given temperature, it has not been possible to produce charges displaying the same fS_2 and fO_2 but with widely

different iron-melt contents. Only charges belonging to the MP12 and MP7 series (Table 5) are suitable to test the effect of varying iron content on sulphur solubility under quasi-constant fS_2 and fO_2, albeit for iron content below 1 wt % only. These charges also display a negative trend between iron and sulphur in melt. Such a negative correlation is corroborated by the iron-rich but sulphur-poor melt in all magnetite-doped charges (Table 5). Altogether, the above lines of evidence demonstrate unequivocally that an iron-rich rhyolite will not dissolve more sulphur than a iron-poor one under the experimental conditions explored here—a result that is at variance with what has been found in mafic melts (e.g. Haughton *et al*., 1974). Clearly, addition of sulphur to a silicic magma in the stability field of sulphide has the main effect of crystallizing sulphide, which removes both iron and sulphur from the melt (and fluid). This scavenging of sulphur results in low fS_2, as long as there is enough iron to produce pyrrhotite. One reason for the fundamental difference between mafic and felsic melts is that the liquidus temperature of S-free hydrous silicic melts is much lower than that of dry mafic melts. Experiments performed in mafic systems were performed at about 1200°C, where much of the iron remains in solution in the melt and where it may complex with sulphur, preventing extensive crystallization of either sulphide or oxides. In contrast, the experiments of the present study are performed at temperatures well below the liquidi of sulphides, as indicated by their occurrence in nearly all run products. It is mostly when fO_2 > NNO+1·5, or in the anhydrite stability field, that the negative trend observed between FeO and sulphur solubility becomes weaker, indicating conditions less appropriate for sulphide crystallization (Fig. 5). We note, in addition, that most of the 1 bar experiments investigated the sulphur behaviour without the involvement of H-bearing species (e.g. O'Neill & Mavrogenes, 2002), and, thus, the solubility mechanisms of sulphur in those studies are probably different from those proposed here.

The foregoing considerations show that the application of the present thermodynamic model to melt compositions other than metaluminous rhyolite, in particular to more mafic compositions, is not warranted. Studies carried out on the H_2O and CO_2 solubilities in various silicate-melt compositions have shown that the thermodynamic parameters, i.e. enthalpy of species dissolution and its partial molar volume, are strongly dependent on melt composition (see Holloway & Blank, 1994). This stems from the fact that dissolution mechanisms, and, thus, the energetics of solution, may widely vary with melt composition. An obvious difference is that sulphur may complex with iron in melts with higher FeO contents than those of the present study, which may lead to significantly different solution parameters. Another example concerns the alkalis over alumina balance (i.e. peralkaline, peraluminous) which evidently affects the proportion of O^{2-} and, thus, the sulphur behaviour. Therefore, although the thermodynamic model appears to reproduce successfully first-order observations bearing on the sulphur behaviour in silicate melts, its quantitative use on melt compositions other than metaluminous rhyolite requires prior experimental investigation of ΔH and V_i values associated with any given melt composition.

The effect of temperature on the solubility of sulphur and its speciation

Temperature appears to exert a positive effect on the solubility of H_2S—a behaviour at variance with that of both CO_2 and H_2O, at least in the low-pressure range, whereas SO_2 appears to be less sensitive to this parameter. As Stolper *et al*. (1987) have emphasized,

the bulk effect of temperature on volatile solubility in silicate melts is controlled by the energetic balance between the reactions controlling molecular (e.g. H_2S, SO_2, H_2O, CO_2) and anion groups' solubility (e.g. HS^-, SO_4^{2-}, OH^-, CO_3^{2-}). In general, the solubility of molecular species decreases with *T* (Stolper *et al*., 1987; Fogel & Rutherford, 1990), whereas the abundance of species formed by reaction with the melt is enhanced by temperature (see Zhang, 1999). Thus, the fact that under reduced conditions, the bulk sulphur solubility has a strong and positive temperature dependence might be interpreted as the dominant presence of S^{2-} or HS^- species over molecular H_2S in rhyolite melts, i.e. that, essentially, all dissolved H_2S reacts with the aluminosilicate melt framework to yield HS^- units. Our data favor a reaction such as (15), in which exchange between gaseous H_2S and hydroxyl groups is the dominant mechanism of sulphur incorporation into hydrous and iron-poor silicate melts. At high fO_2, it is not yet possible to decipher the details of the solution reaction but if all SO_2 reacts with hydroxyl groups to form SO_4^{2-} units, then it might be expected that there is a positive effect of temperature on solubility under oxidizing conditions as well. Thus, compared with H_2O and CO_2, which dissolve both physically and chemically, the case for sulphur is different, as its dissolution seems to proceed dominantly chemically, by reaction of gaseous species with the melt framework, keeping the abundance of molecular species at a marginal level. Another major difference is that, as far as we know, for fixed melt chemistry, both H_2O and CO_2 speciations are insensitive to redox conditions, whereas, clearly, this parameter is the major controlling factor of sulphur speciation in silicate melts.

Although significant, the dependence on temperature appears to be low compared with the effects exerted by fO_2 and fS_2. Below NNO, the temperature dependence established in other studies performed on hydrous silicic melts (Carroll & Rutherford, 1987; Luhr, 1990) is lower than that reported here. For instance, the experiments of Luhr (1990) on the El Chichòn trachyandesite show almost no effect of temperature on the melt S content between 800 and 1000°C at an fO_2 buffered by the quartz–fayalite–magnetite solid buffer (NNO–0·7). In contrast, at high fO_2, a strong positive temperature dependence has been evidenced by both Carroll & Rutherford (1987) and Luhr (1990). In these experiments, however, low-temperature runs are largely below the liquidus of the bulk composition used as starting material, which means that the residual melt composition changes significantly with rising temperature, unlike in the present study. In such experiments, the temperature effect on sulphur solubility may thus be hindered by the interplay of additional variables such as $aSiO_2$ or fS_2, even when performed at fixed redox conditions. Thus, it remains to be demonstrated whether the strong positive temperature dependence of sulphur solubility observed under oxidizing conditions in hydrous silicic melts by Carroll & Rutherford (1987) and Luhr (1990) is, indeed, solely because of temperature, or the combined effects of varying melt composition with temperature in addition to varying fS_2.

The effect of pressure

The last parameter of interest is pressure. Recent experimental studies have confirmed the earlier findings of Wendlant (1982) that pressure decreases the sulphur solubility in dry mafic systems (Mavrogenes & O'Neill, 1999; Holzheid & Grove, 2002). By contrast, in hydrous systems, Luhr (1990) concluded that pressure has an opposite effect.

Nevertheless, as for temperature, the experiments of Luhr (1990) in which pressure was varied involved also varying other parameters, in particular the melt composition, and it cannot be ruled out that the observed increase in S_{melt} also reflects a change in melt chemistry and not only an intrinsic and positive effect of pressure. Our experiments suggest that one of the controlling parameters of sulphur solubility in H-bearing systems is fH_2S. By analogy with what happens with water, as total pressure decreases, fH_2S will decrease too, so that the melt sulphur solubility should decrease eventually, in keeping with the Henrian behaviour shown above. In support of this are the experiments of Katsura & Nagashima (1974), which show that a rhyodacite melt (66·7 wt % SiO_2) equilibrated at 1 bar and 1250°C, with an H–C–S–O gas mixture over an fO_2 range of NNO–5 to NNO+5, displays sulphur concentration always below 50 ppm. Thus, given that natural silicic magmas have eruption temperatures that are 300–400°C lower, and that they have higher silica contents than the rhyodacite experimental melts, it can be anticipated that their equilibrium sulphur concentration at near atmospheric conditions is close to the ppm level. That, at 1 bar, silicic compositions have much lower sulphur solubility than mafic ones is related to the fact that, under anhydrous conditions, the proportion of O^{2-} is significantly higher in the latter than in the former.

Application of the empirical model

The empirical model can be tested by applying it to eruption products for which common pre-eruptive parameters are well known (P, T, fO_2) in addition to fS_2 and the melt-sulphur concentration. These include the Bishop Tuff (0·76 Ma), Krakatau (1885), Katmai (1912), Mt St Helens (1980) and El Chichòn (1982) eruptions. Pre-eruptive parameters, as well as calculated melt-sulphur fugacities, are listed in Table 6. Equation (25) reproduces observed sulphur fugacities to within 1 log unit, except for Mt St Helens. The origin of the disagreement for Mt St Helens might be because of the relatively low sulphur content measured, close to the detection limit of EMPA: if, for instance, a pre-eruptive melt-sulphur content of 100 ppm is assumed, then the calculated ΔFFS is 7·78, or within 0·2 log units of the measured one by the pyrrhotite composition (Whitney, 1984). As the experimental melt compositions are metaluminous and because of the empirical nature of equation (25), the model should not be applied to either peraluminous or peralkaline rhyolites.

SUMMARY

(1) Experiments with controlled fO_2 and fS_2 have been performed in the temperature range 800–1000°C on rhyolite-melt compositions, to establish the effect of those variables on the solubility of sulphur. The fS_2 was measured either by the pyrrhotite (fO_2 < NNO+1) or by the fluid phase (fO_2 > NNO+1·5) compositions, using for the latter an MRK equation of state.

(2) At fO_2 < NNO+1 and temperatures of <1000°C, the addition of iron to a sulphur-bearing rhyolite melt promotes massive crystallization of pyrrhotite, which consequently removes most of the sulphur from the melt.

(3) At constant fO_2, the sulphur solubility increases with fS_2. Below NNO+1, there is a linear relationship between the melt-sulphur concentration and fH_2S, whereas above NNO+1, fSO_2 seems the dominant controlling factor.

(4) The sulphur solubility in rhyolite melts is a result of the dissolution of both H_2S and SO_2 fluid species. The strong positive dependence of solubility on temperature observed at fO_2 < NNO+1 suggests that the abundance of dissolved molecular H_2S is low and that most of the sulphur dissolves by chemical reaction with the aluminosilicate framework. SO_2 possibly behaves similarly but this needs to be checked by additional experimental work, with a more precise control of fS_2 under oxidizing conditions than that achieved in the present work.

(5) A simple thermodynamic model can be developed, adopting an approach similar to that used for modelling the solubilities of both H_2O and CO_2 in silicate melts. This model reproduces first-order observations concerning the sulphur solubility and speciation in silicate melts. Yet, there is an urgent need for rigorously determining the nature and abundance of different sulphur species dissolved in melts and their dependence on melt composition.

(6) An empirical model for metaluminous rhyolites that is easier to handle has been developed also. It may be used primarily to determine the fS_2 of common metaluminous silicic arc magmas.

ACKNOWLEDGEMENTS

This paper is a part of the PhD thesis of the first author. The experimental work has been partly financed by the ENV4-CT96-0259 CE programme. Helpful comments were provided by Malcolm Rutherford on an early version of the manuscript. Thorough and helpful reviews of Jake Lowenstern, Leslie Baker and an anonymous reviewer are gratefully acknowledged.

REFERENCES

Abraham, K. P. & Richardson, F. D. (1960). Sulphide capacities of silicate melts. Part II. Journal of the Iron & Steel Institute 196, 313–317.

Abraham, K. P., Davis, M. W. & Richardson, F. D. (1960). Sulphide capacities of silicate melts. Part I. Journal of the Iron & Steel Institute 196, 309–312.

Ancey, M., Basternaire, F. & Tixier, R. (1978). Application des methodes statistiques en microanalyse. In: Physique, E. D. (ed.) Microanalyse, microscope electronique a` balayage. Orsay: Edition de physique, Universitée d'Orsay, pp. 323–347.

Anderson, A. T., Newman, S., Williams, S. N., Druitt, T. H., Skirius, C. & Stolper, E. (1989). H2O, CO2, Cl gas in Plinian and ash-flow Bishop rhyolite. Geology 17, 221–225.

Arnold, R. G. & Reicher, L. E. (1962). Measurement of the metal content of naturally occurring, metal deficient, hexagonal pyrrhotite by an X-Ray spacing method. American Mineralogist 47, 105–111.

Baker, L. I. & Rutherford, M. J. (1996a). Sulphur diffusion in rhyolite melts. Contributions to Mineralogy and Petrology 123, 335–344.

Baker, L. I. & Rutherford, M. J. (1996b). The effect of dissolved water on the oxidation state of silicic melts. Geochimica et Cosmoschimica Acta 60, 2179–2187.

Blank, J., Stolper, E. M. & Carroll, M. (1993). Solubilities of carbon dioxide and water in rhyolitic melt at 850_C and 750 bars. Earth and Planetary Science Letters 119, 27–36.

Boorman, R. S. (1967). Subsolidus studies in the ZnS–FeS–FeS2 system. Economic Geology 62, 614–631.

Breedveld, G. J. F. & Prausnitz, J. M. (1973). Thermodynamic properties of supercritical fluids and their mixture at very high pressures. AIChE Journal 19, 783–796.

Buchanan, D. L. & Nolan, J. (1979). Solubility of sulphur and sulphide immiscibility in synthetic tholeiitic melts and their relevance to Bushveld-complex rocks. Canadian Mineralogist 17, 483–494.

Buchanan, D. L., Nolan, J., Wilkinson, N. & De Villiers, J. P. R. (1983). An experimental investigation of sulfur solubility as a function of temperature in silicate melts. Special Publication of the Geological Society of South Africa 7, 383–391.

Burnham, C. W. (1979). The importance of volatiles consituents. In: Yoder, H. S. (ed.) The Evolution of the Igneous Rocks: Fiftieth Anniversary Perspectives. Princeton, NJ: Princeton University Press, pp. 439–482.

Burnham, C. W., Holloway, J. R. & Davis, N. F. (1969). Thermodynamic properties of water to 1000°C and 10 000 bars. Geological Society of America, Special Paper 132, 1–96.

Carroll, M. R. & Rutherford, M. J. (1985). Sulphide and sulphate saturation in hydrous silicate melts. Journal of Geophysical Research 90, C601–C612.

Carroll, M. R. & Rutherford, M. J. (1987). The stability of igneous anhydrite: experimental results and implications for sulphur behavior in the 1982 El Chichon trachyandesite and other evolved magmas. Journal of Petrology 28, 781–801.

Carroll, M. R. & Rutherford, M. J. (1988). Sulphur speciation in hydrous experimental glasses of varying oxidation state: results from measured wavelength shifts of sulphur X-rays. American Mineralogist 73, 845–849.

Carroll, M. R. & Webster, J. D. (1994). Solubilities of sulfur, noble gases, nitrogen, chlorine, and fluorine in magmas. In: Holloway, J. R. & Carroll, M. R. (eds) Volatiles in Magmas. Mineralogical Society of America, Reviews in Mineralogy 30, 231–280.

Connolly, J. A. & Cesare, B. (1993). C–O–H–S fluid composition and oxygen fugacity in graphitic metapelites. Journal of Metamorphic Geology 11, 379–388.
Devine, J. D., Gardner, J. E., Brack, H. P., Layne, G. D. & Rutherford, M. J. (1995). Comparison of microanalytical methods for estimation of H2O contents of silicic volcanic glasses. American Mineralogist 80, 319–328.
Ferry, J. M. & Baumgartner, L. (1987). Thermodynamic models of molecular fluids at the elevated pressures and temperatures of crustal metamorphism. In: Carmichael, I. S. E. & Eugster, H. P. (eds)
Reviews in Mineralogy. Mineralogical society of America, 323–365. Fincham, C. J. B. & Richardson, F. D. (1954). Behaviour of sulphur in silicate and aluminate melts. Proceedings of the Royal Society of London 223, 40–62.
Fogel, R. A. & Rutherford, M. J. (1990). The solubility of carbon dioxide in rhyolitic melts: a quantitative FTIR study. American Mineralogist 75, 1311–1326.
Froese, E. & Gunter, A. E. (1976). A note on the pyrrhotite-sulphur vapor equilibrium. Economic Geology 71, 1589–1594.
Gaillard, F., Scaillet, B., Pichavant, M. & B_eny, J. M. (2001). The effect of water and fO2 on the ferric–ferrous ratio of silicic melts. Chemical Geology 174, 255–273.
Haughton, D. R., Roeder, P. L. & Skinner, B. J. (1974). Solubility of sulphur in mafic magmas. Economic Geology 69, 451–466.
Hildreth, W. (1979). The Bishop Tuff: evidence for the origin of compositional zonation in silicic magma chambers. In: Chapin, C. E. & Elston, W. E. (eds) Ash-flow Tuffs. Geological Society of America, Special Paper 180, 43–75.
Hildreth, W. (1983). The compositionally zoned eruption of 1912 in the Valley of Ten Thousand Smokes, Katmai National Park, Alaska. Journal of Volcanology and Geothermal Research 18, 1–56.
Holloway, J. R. (1977). Fugacity and activity of molecular species in supercritical fluids. In: Fraser, D. (ed.) Thermodynamics in Geology. Boston, MA: Kluwer Academic, pp. 161–181.
Holloway, J. R. (1981). Volatile interactions in magmas. In: Newton, R. C., Navrotsky, A. & Wood, B. J. (eds) Thermodynamics of Minerals and Melts. Advances in Physical Geochemistry 1, 273–283.
Holloway, J. R. (1987). Igneous fluids. In: Thermodynamic Modelling of Geological Materials: Minerals, Fluids and Melts. Mineralogical society of America, Reviews in Mineralogy 17, 211–232.
Holloway, J. R. & Blank, J. (1994). Application of experimental results to C–O–H species in natural melts. In: Holloway, J. R. & Carroll, M. R. (eds) Volatiles in Magmas. Mineralogical society of America, Reviews in Mineralogy 30, 187–230.
Holloway, J. R., Pan, V. & Gudmundsson, G. (1992). High-pressure fluid-absent melting experiments in the presence of graphite: oxygen fugacity, ferric/ferrous ratio and dissolved CO2. European Journal of Mineralogy 4, 105–114.
Holzheid, A. & Grove, T. L. (2002). Sulfur saturation limits in silicate melts and their implications for core formation scenarios for terrestrial planets. American Mineralogist 87, 227–237.
Katsura, T. & Nagashima, S. (1974). Solubility of sulphur in some magmas at 1 atmosphere. Geochimica et Cosmochimica Acta 38, 517–531.
Keppler, H. (1999). Experimental evidence for the source of excess sulfur in explosive volcanic eruptions. Science 284, 1652–1654.

Kucha, H., Wouters, R. & Arkens, O. (1989). Determination of sulphur and iron valence by microprobe. Scanning Microscopy 3, 89–97.
Kullerud, G. (1971). Experimental techniques in dry sulphide research. In: Ulmer, G. C. (ed.) Research Techniques for High Pressure and High Temperature. New York: Springer Verlag, pp. 288–315.
Lowenstern, J. B. (1993). Evidence for a copper-bearing fluid in magma erupted at the Valley of Ten Thousand Smokes, Alaska. Contributions to Mineralogy and Petrology 114, 409–421.
Luhr, J. F. (1990). Experimental phase relations of water- and sulphursaturated arc magmas and the 1982 eruptions of El Chichon Volcano. Journal of Petrology 31, 1071–1114.
Luhr, J. F., Carmichael, I. S. E. & Varekamp, J. C. (1984). The 1982 eruptions of El Chich_on Volcano, Chiapas, Mexico: mineralogy and petrology of the anhydrite-bearing pumices. Journal of Volcanology and Geothermal Research 23, 69–108.
Mandeville, C. W., Carey, S. & Sigurdsson, H. (1996). Magma mixing, fractional crystallisation and volatile degassing during the 1883 eruption of Krakatau volcano, Indonesia. Journal of Volcanology and Geothermal Research 74, 243–274.
Mandeville, C. W., Sasaki, A., Saito, G., Faure, K., King, R. & Hauri, E. (1998). Open-system degassing of sulphur from Krakatau 1883 magma. Earth and Planetary Science Letters 160, 709–722.
Martel, C., Pichavant, M., Bourdier, J. L., Traineau, H., Holtz, F. & Scaillet, B. (1998). Magma storage conditions and control of eruption regime in silicic volcanoes: experimental evidence from Mt. Pelee. Earth and Planetary Science Letters 156, 89–99.
Mavrogenes, J. A. & O'Neill, H. S. C. (1999). The relative effects of pressure, temperature and oxygen fugacity on the solubility of sulfide in mafic magmas. Geochimica et Cosmochimica Acta 63, 1173–1180.
Mysen, B. & Popp, R. K. (1980). Solubility of sulfur in CaMgSi2O6 and NaAlSi3O8 melts at high pressure and temperature with controlled fO2 and f S2. American Journal of Science 280, 78–92.
Nagashima, S. & Katsura, T. (1973). The solubility of sulfur in Na2O–SiO2 melts under various oxygen partial pressures at 1200, 1250 and 1300_C. Bulletin of Chemistry of the Japanese Society 46, 3099–3103.
Ohmoto, H. & Kerrick, D. M. (1977). Devolatilization equilibria in graphitic systems. American Journal of Science 277, 1013–1044.
O'Neill, H. S. C. & Mavrogenes, J. A. (2002). The sulfide capacity and the sulfur content at sulfide saturation of silicate melts at 1400°C and 1 bar. Journal of Petrology 43, 1049–1087.
Pichavant, M. (1987). Effects of B and H2O on liquidus phase relations in the haplogranite system at 1 kbar. American Mineralogist 72, 1056–1070.
Pitzer, K. S. & Sterner, S. M. (1994). Equation of state valid continuously from zero to extreme pressures for H2O and CO2. Journal of Chemical Physics 101, 3111–3116.
Pownceby, M. I. & O'Neill, H. S. C. (1994). Thermodynamic data from redox reactions at high temperatures. III: Activity–composition relations in Ni–Pd alloys from EMF measurements at 850–1250 K, and calibration of the NiOþNi–Pd assemblages as a redox sensor. Contributions to Mineralogy and Petrology 116, 327–339.
Richardson, F. D. & Fincham, C. J. B. (1954). Sulphur in silicate and aluminate slags. Journal of the Iron & Steel Institute 178, 4–15. Richardson, F. D. &Withers, G. (1950).

Thermodynamic aspects of the movement of sulphur between gas and slag in the basic open-hearth process. Journal of the Iron & Steel Institute 165, 66–71.
Ricke, W. (1960). Ein Beitrag zur Geochemie des Schwefels. Geochimica and Cosmochimica Acta 21, 35–80.
Robie, R. A., Hemingway, B. S. & Fisher, J. R. (1979). Thermodynamic properties of minerals and related substances at 298.15K and 1 bar (105 Pa) pressure and at higher temperatures. US Geological Survey Bulletin 1452.
Roux, J. & Volfinger, M. (1996). Mesures pr_ecises a` l'aide d'un detecteur courbe. Journal de Physique IV 6, C4-127–C4-134.
Rutherford, M. J., Sigurdsson, H., Carey, S. & Davis, A. (1985). The May 18, 1980, eruption of Mount St. Helens 1. Melt composition and experimental phase equilibria. Journal of Geophysical Research 90, 2929–2947.
St Pierre, G. R. & Chipman, J. (1956). Sulfur equilibria between gases and slags containing FeO. Transactions of the Metallurgical Society of AIME 206, 1474–1483.
Scaillet, B. & Evans, B. W. (1999). The June 15, 1991 eruption of Mount Pinatubo. I. Phase equilibria and pre-eruption P–T–fO2–f H2O conditions of the dacite magma. Journal of Petrology 40, 381–411.
Scaillet, B., Pichavant, M., Roux, J., Humbert, G. & Lefevre, A. (1992). Improvements of the Shaw membrane technique for measurement and control of f H2 at high temperatures and pressures. American Mineralogist 77, 647–655.
Scaillet, B., Clemente, B., Evans, B. W. & Pichavant, M. (1998). Redox control of sulfur degassing in silicic magmas. Journal of Geophysical Research 103, 23937–23949.
Schneider, A. (1970). The sulphur isotopic composition of basaltic rocks. Contributions to Mineralogy and Petrology 25, 95–124.
Shaw, H. R. (1963). Hydrogen–water vapour mixtures: control of hydrothermal experiments by hydrogen osmosis. Science 139, 1220–1222.
Shi, P. & Saxena, S. K. (1992). Thermodynamic modeling of the C–O–H–S fluid system. American Mineralogist 77, 1220–1222.
Shima, H. & Naldrett, A. J. (1975). Solubility of sulphur in an ultramafic melt and relevance of the system Fe–S–O. Economic Geology 70, 960–967.
Spera, F. J. & Bergman, S. C. (1980). Carbon dioxide in igneous petrogenesis: I aspects of the dissolution of CO2 in silicate liquids. Contributions to Mineralogy and Petrology 74, 55–66.
Stolper, E. M. (1982). Water in silicate glasses: an infrared spectroscopic study. Contributions to Mineralogy and Petrology 81, 1–17.
Stolper, E. M., Fine, G. J., Johnson, T. & Newman, S. (1987). The solubility of carbon dioxide in albitic melts. American Mineralogist 72, 1071–1085.
Taylor, J. R., Wall, V. J. & Pownceby, M. I. (1992). The calibration and application of accurate redox sensors. American Mineralogist 77, 284–295.
Toulmin, P. I. & Barton, P. B. J. (1964). A thermodynamic study of pyrite and pyrrhotite. Geochimica et Cosmochimica Acta 28, 641–671.
Turkdogan, E. T. & Pearce, M. L. (1963). Kinetics of sulphur reaction in oxide melt–gas system. Transactions of the Metallurgical Society of AIME 227, 940–949.
Wendlant, R. F. (1982). Sulfide saturation of basalt and andesite melts at high pressures and temperatures. American Mineralogist 67, 877–885.
Westrich, H. R., Eichelberger, J. C. & Hervig, R. L. (1991). Degassing of the 1912 Katmai magmas. Geophysical Research Letters 18, 1561–1564.

Whitney, J. A. (1984). Fugacities of sulphurous gases in pyrrhotitebearing silicic magmas. American Mineralogist 69, 69–78.
Winther, K. T., Watson, E. B. & Korenowski, G. M. (1998). Magmatic sulphur compounds and sulphur diffusion in albite melt at 1GPa and 1300–1500°C. American Mineralogist 83, 1141–1151.
Yund, R. A. & Hall, H. T. (1969). Hexagonal and monoclinic pyrrhotites. Economic Geology 64, 420–423.
Zhang, Y. (1999). H2O in rhyolitic glasses and melts: measurement, speciation, solubility, and diffusion. Reviews of Geophysics 37, 493–516.